



New chronological constraints for the Plio-Pleistocene section of Dhar Iroumyane (Morocco) and the associated fossil locality of Guefaït-4

M. Duval ^{a,b,c,*}, T. Fujioka ^a, H. Haddoumi ^d, J.M. Parés ^a, H. Aouraghe ^d,
 A. Churruca Clemente ^a, J. Lachner ^e, G. Rugel ^e, K. Stübner ^e, M. del Val ^a,
 S. Pla-Pueyo ^f, H. Mhamdi ^d, M. Souhir ^d, M. Farkouch ^{d,i,j}, J. Van der Made ^g,
 P. Piñero ^{i,j}, J. Agustí ^{i,j}, A. Rodríguez-Hidalgo ^{i,k}, M.G. Chacón ^{i,j,l,m,n},
 R. Sala-Ramos ^{i,j}

^a Geochronology and Geology, Centro Nacional de Investigación Sobre la Evolución Humana (CENIEH), Burgos, Spain

^b Australian Research Centre for Human Evolution (ARCHE), Griffith University, Nathan, Australia

^c Palaeoscience Labs, Dept. Archaeology and History, La Trobe University, Melbourne, Australia

^d Université Mohamed Premier, Faculté des Sciences, Département de Géologie, avenue Mohamed 6, Quartier al Qods, 60 000, Oujda, Morocco

^e Helmholtz-Zentrum Dresden-Rossendorf, Dresden, Germany

^f Dpto. de Didáctica de las Ciencias Experimentales. Facultad de Ciencias de la Educación, Universidad de Granada. Campus de Cartuja, s/n, 18071, Granada, Spain

^g Museo Nacional de Ciencias Naturales, Consejo Superior de Investigaciones Científicas, c. José Gutiérrez Abascal 2, 28006, Madrid, Spain

^h Departament de Botànica i Geologia, Universitat de València, Doctor Moliner 50, Burjassot, 46100, Spain

ⁱ Institut Català de Paleoecología Humana i Evolució Social (IPHES-CERCA), Zona Educacional 4, Campus Sescelades Edifici W3, 43007, Tarragona, Spain

^j Universitat Rovira i Virgili (URV), Departament D'Història i Història de l'Art, Av. Catalunya, 35, 43002, Tarragona, Spain

^k Instituto de Arqueología, Mérida (IAM), Consejo Superior de Investigaciones Científicas-Junta de Extremadura, Mérida, Spain

^l Seminari d'Estudis i Recerques Prehistòriques (SERP), Universitat de Barcelona, 6-8 Montalegre St, 08001 Barcelona, Spain

^m Institut d'Arqueologia de la Universitat de Barcelona (IAUB), 6-8 Montalegre St, 08001 Barcelona, Spain

ⁿ UMR7194-HNHP (MNHN-CNRS-UPVD-Sorbonne Universités), Musée de l'Homme, 17 Place Du Trocadéro, 75116, Paris, France

A B S T R A C T

We provide new numerical age constraints to the Plio-Pleistocene section of Dhar Iroumyane (Morocco) and the associated fossil locality of Guefaït-4, which has yielded an exceptionally rich and diverse faunal assemblage, through a combination of Electron Spin Resonance (ESR) and Terrestrial Cosmogenic Nuclides (TCN) dating of quartz. While challenging in many aspects, the application of these dating methods to the same deposits located about 5 m below the fossiliferous horizon returns consistent numerical dating results within respective uncertainties. More specifically, the age overlap enables to propose a combined ESR-TCN age of 2.87 ± 0.11 Ma (1σ), which may be regarded a maximum age constraint for Guefaït-4 from a chronostratigraphic point of view. These results allow us to narrow down the options of chronological interpretation proposed in a previous study by Parés et al. (2023), by supporting a correlation of the magnetic reversals initially identified a few meters above the site to the Gauss-Matuyama transition (2.61 Ma). A final age estimate of ~ 2.7 Ma may be inferred for the fossil horizon through a series of sensitivity tests based on sedimentation rates. With this approach, the normal polarity interval identified in the upper part of the sequence is most likely correlated to the Olduvai Subchron (1.93–1.78 Ma), and the two short reversals in the lowermost deposits with dominantly normal polarity may be reasonably associated to the intra-Gauss Mammoth (3.33–3.21 Ma) and Kaena (3.12–3.03 Ma) Subchrons. Consequently, the present work help position Guefaït-4 as a key Late Pliocene fossil locality in N Africa for the establishment of a robust regional Plio-Pleistocene biochronology, although further work is required in the future to increase the chronological resolution along the sedimentary sequence. While we do acknowledge the intrinsic uncertainty associated with the ESR and TCN dating results (including the limited number of samples processed in the present study), these encouraging results nevertheless illustrate the interest of using a multi-technique approach to constrain Plio-Pleistocene deposits, and the importance of combining numerical dating with magnetostratigraphy and biostratigraphy/biochronology in non-volcanic sedimentary context. Such approach also contributes to a better understanding of the potential and limitations of each dating method, and helps providing critical insights into the avenues worth exploring in the future from a methodological and sampling point of view in order to ensure future successful ESR and TCN dating applications beyond 2 Ma.

* Corresponding author. Centro Nacional de Investigación Sobre la Evolución Humana (CENIEH), Burgos, Spain.

E-mail address: mathieu.duval@cenieh.es (M. Duval).

1. Introduction

In contrast to other regions of the continent, North Africa shows a limited number of chronologically well-constrained Plio-Pleistocene fossil localities by means of numerical dating methods. This lack is especially pronounced for the Pliocene and Early Pleistocene fossil record (see an overview in Stoetzel (2013), Van der Made et al., 2021, Werdelin (2010) and references therein), despite noticeable efforts in the most recent years (e.g., Gallotti et al., 2021; Sahnouni et al., 2018; Duval et al., 2021, 2023). In this context, the recently-described 134 m-thick Dhar Iroumyane section, NE Morocco, is crucial to contribute filling this gap of knowledge (Parés et al., 2023). In particular, this section includes the fossil locality known as Guefaït-4, which has provided a rich fossil assemblage made of large and small mammals (e.g., Alba et al., 2021; Piñero et al., 2020; Madurell-Malapeira et al., 2021; Van der Made et al., in prep.). Based on a combination of palaeomagnetism and biochronology, Parés et al. (2023) tentatively anchored the fossil horizon to the late Gauss chron (3.60–2.61 Ma; the age of the Geomagnetic Polarity Time Scale (GPTS) is taken from Raffi et al., 2020), despite the inconclusive, or apparently incompatible preliminary independent age control initially given by Electron Spin Resonance (ESR) and combined Uranium-series/ESR methods applied to optically-bleached quartz grains and fossil teeth. In this context, subsequent fieldwork campaigns were organised and new samples were specifically collected for a combined numerical dating approach using ESR and Terrestrial Cosmogenic Nuclides (TCN) methods, in order to refine and strengthen this first chronostratigraphic framework. These new dating results are presented and discussed hereafter.

2. General context

The High Plateaus (or Rekkame high plateau), Guercif, and Missour Basins, in northern Morocco, are large intramontane depressions filled up by Neogene and Quaternary sediments (e.g., Pastor et al., 2015 and references therein). For the most part, these sediments remain barely deformed and generally horizontal/subhorizontal, and therefore they offer great opportunities to better understand paleoenvironmental changes in Northern Africa during the Cenozoic and Quaternary, if properly dated. The multi-disciplinary investigations carried out by a joint Moroccan-Spanish team over the last eighteen years in the Ain Beni Mathar basin (Jerada Province, High Plateaus, NE Morocco) led to the discovery of numerous Plio-Pleistocene archaeo-palaeontological localities (e.g., Sala-Ramos et al., 2022 and references therein), including Guefaït-4. The fossiliferous horizon was identified on a steep side of a flat-topped elevation located near the town of Guefaït (also known as Gafaït, Gafait or Guefai), in the north-western extremity of the Za River basin, which is part of the larger Moulouya River catchment (Fig. 1). Initial lithostratigraphic and magnetostratigraphic study of various sections from the slopes of the mesa eventually led to the establishment of the 134 m-thick Dhar Iroumyane composite section (see details in Parés et al., 2023).

The lithostratigraphy of Dhar Iroumyane may be divided into four main units numbered 1 to 4 from bottom to top (Figs. 1 and 2; see Parés et al., 2023 for further details). Unit 1 is at least 70 m-thick, and made of alternating red lutites, sandstones and polymictic conglomerates interpreted as to alluvial and fluvial fan system deposits. Overlying Unit 2 marks a significant change of depositional environment, dominated by grey 4 m-thick marls and marly limestone sediments, well visible in the landscape (Figs. 1 and 2) and interpreted as distal fluvio-lacustrine deposits (see also Supplementary Information of Ramírez-Pedraza et al., 2024). The top of this unit is defined by a laterally-continuous limestone bed (named as Limestone C) bearing casts of large fossil gastropods, which constitutes an excellent marker bed for short-distance lithostratigraphic correlations. Unit 3 is made by a 40–45 m-thick succession of red fine-grained clastic sediments interbedded with some conglomerate lenses, while the uppermost stratigraphic Unit 4 has 30 m of

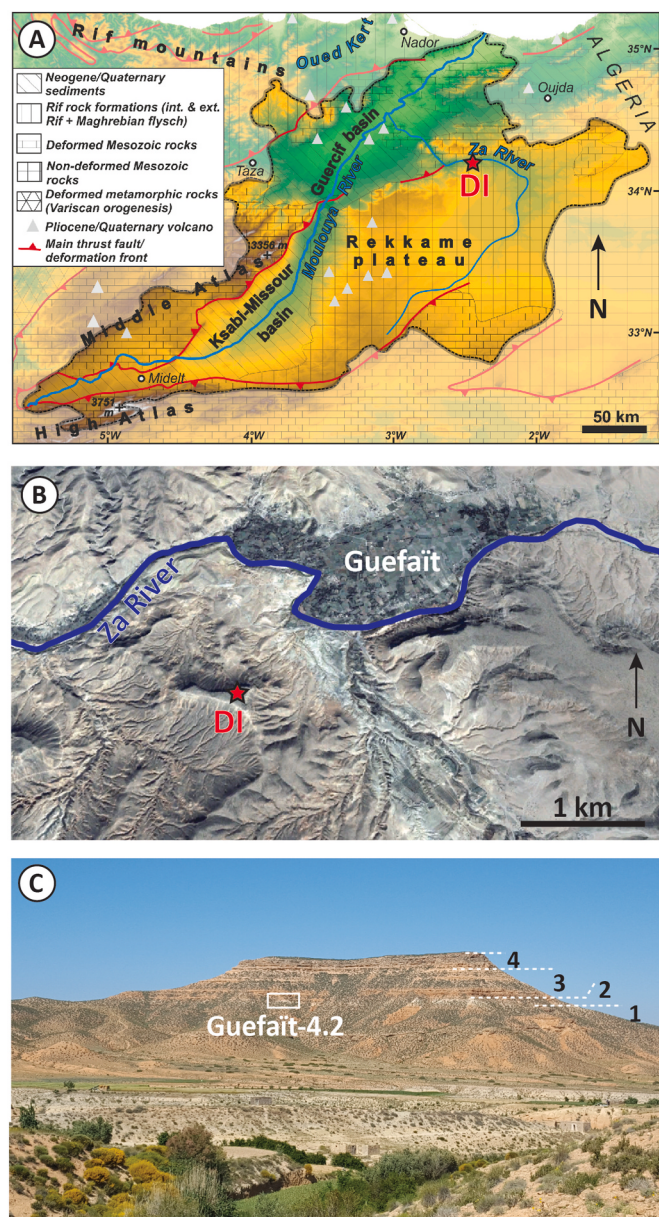


Fig. 1. General context. A: Map of the Moulouya River catchment (delimited by black dashed line), with the main regional geological structures of northern Morocco (modified from Rixhon et al., 2017). The location of the Dhar Iroumyane (DI) section is indicated by the red star. B: Aerial view of the area around the town of Guefaït, Morocco (Source: Google Earth). Dhar Iroumyane (DI) section (red star) corresponds to the flat-topped elevation at the SW of Guefaït. C: View of the flat-topped elevation from the East. The position of the fossil site Guefaït-4.2. is indicated, as well as the various lithostratigraphic units identified by Parés et al. (2023). (For interpretation of the references to colour in this figure legend, the reader is referred to the Web version of this article.)

whitish micritic limestone with palustrine features, interpreted as an area dominated by shallow, ephemeral water bodies, probably corresponding to wetlands (in the sense of Pla-Pueyo and Gierlowski-Kordesch, 2024) developed on the floodplain of a river.

Lithostratigraphic Unit 2 hosts the fossil horizon Guefaït-4 (GFT-4), discovered in 2015, from where several localities (Guefaït-4.1, 4.2, and 4.3) have been identified. While fossil specimens, and especially small vertebrates, were punctually collected along that level through sporadic excavations (e.g., Piñero et al., 2020), successive campaigns of extensive excavation carried out at Guefaït-4.2. locality in 2017–2019 over a surface of 28 m² returned a total of 3,269 3D spatially-referenced fossil

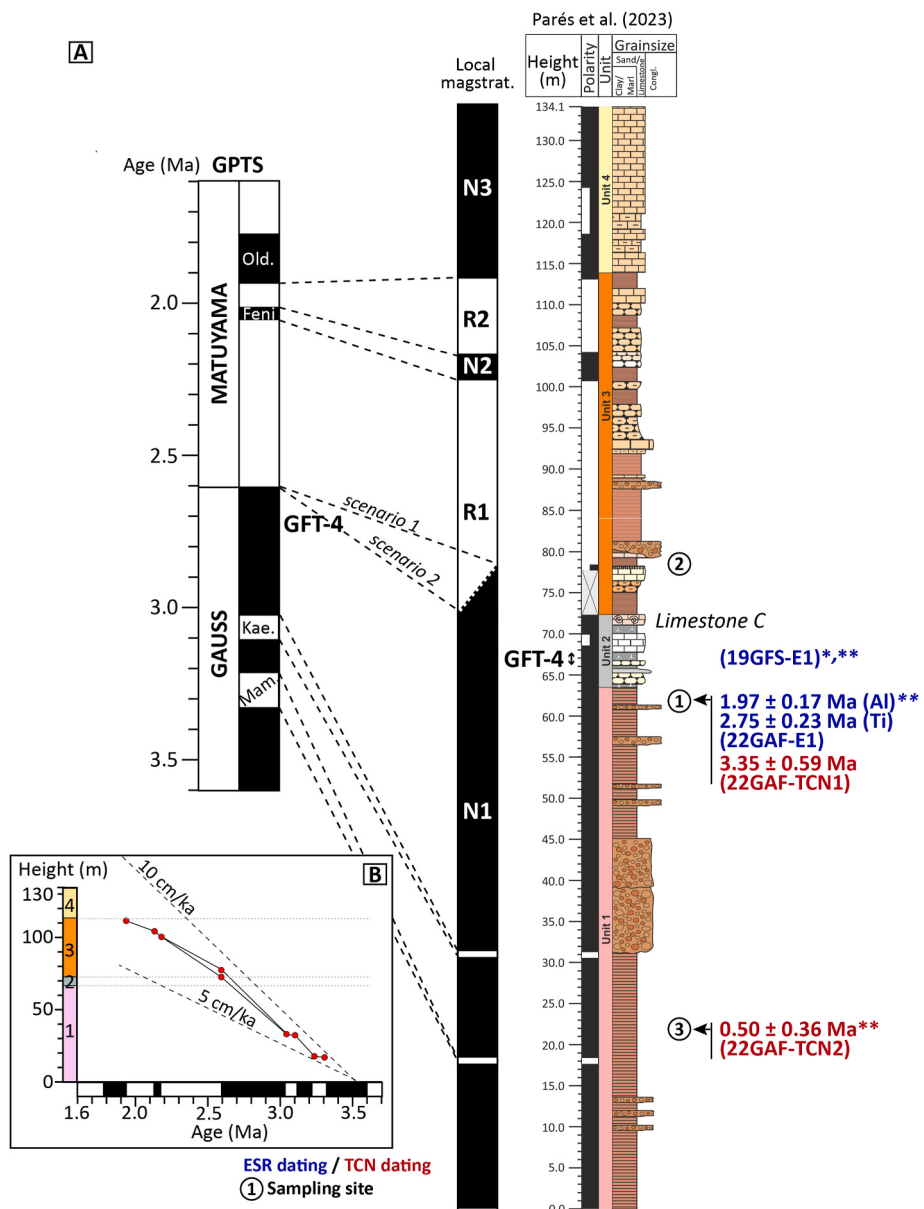


Fig. 2. Overview of the Dhar Iroumyane composite section (modified from Parés et al., 2023): chronostratigraphic framework (A) and Age-Depth model (B). Relative height is expressed against the bottom of the section. The top of the section is located at 933 m above sea level (m.a.s.l.). The position of the three sampling sites (numbered 1 to 3) as well as of the Guefait-4 (GFT-4) fossil horizon is indicated. ESR (blue) and TCN (red) sample ID and dating results are given. ESR sample 22GAF-E2, which did not produce a sufficient amount of purified quartz for dating purpose (see text) is positioned at sampling site 2. Key: * ESR sample dated in Parés et al. (2023); ** Age results whose reliability and/or accuracy may be regarded as questionable (see text for explanations). The age of the geomagnetic chronos and subchrons of the Geomagnetic Polarity Time Scale (GPTS) are taken from Raffi et al. (2020): 3.60–2.61 Ma and 2.61–0.77 Ma for Gauss and Matuyama Chrons, respectively, and 3.33–3.21 Ma, 3.12–3.03 Ma, 2.16–2.12 Ma and 1.93–1.78 Ma for the Mammoth (Mam.), Kaena (Kae.) and Olduvai (Old.) Subchrons. Note that the sediment accumulation rate of the two short reverse excursions within N1 could not be estimated given their low paleomagnetic sampling resolution. (For interpretation of the references to colour in this figure legend, the reader is referred to the Web version of this article.)

remains (Sala Ramos et al., 2022). These remains were attributed to a wide range of macro- and micro-vertebrates (>30 taxa identified in total, see Table 1; e.g., Piñero et al., 2020, Alba et al., 2021, Madurell-Malapeira et al., 2021, Parés et al., 2023; Ramírez-Pedraza et al., 2024), forming one of the most diverse assemblages in the Plio-Pleistocene fossil record of N Africa. Large mammal remains were found concentrated within the lowermost 120 cm deposits of the local section, with no apparent stratigraphic order (Ramírez-Pedraza et al., 2024). In other words, this overall high taxonomic homogeneity suggests that these fossils may correspond to one single depositional event, or possibly various successive events within a reasonably short time (at geological scale). The taphonomic study indicates a natural

accumulation of the macrovertebrate fossil remains, with a limited transport (by water) and surface exposure, before a rapid burial (Ramírez-Pedraza et al., 2024). Finally, a recent multi-proxy study provided some key insights into the palaeoenvironmental context associated to this fossil assemblage, leading to the identification of an overall mosaic environment, with the combined presence of woodlands, open grasslands and wetlands, but within dominantly arid climate conditions with notable seasonal variations of temperature and precipitation that may have impacted the vegetation structure and composition, as well as water availability throughout the year (Ramírez-Pedraza et al., 2024).

Initial chronological constraints for the sedimentary sequence and

Table 1

Updated composition of the fossil assemblage identified from the fossil locality of Guefaït-4.2. (based on Sala-Ramos et al. (2022), Alba et al. (2021), Madurell Malapeira et al. (2021), Parés et al. (2023), Piñero et al. (2020), Ramírez-Pedraza et al. (2024) and Van der Made (unpublished data)). Note that the taxonomy of the large mammal fossil specimens has been recently revised by one of us (JvdM) and full details will be published soon.

Taxa
<i>Anancus osiris</i>
<i>Macaca cf. M. sylvanus</i>
<i>Vulpes</i> sp.
<i>Eucyon</i> aff. <i>Paralias</i> cf. <i>Ictitherium ebu</i>
<i>Dinofelis</i> sp.
<i>Felis</i> sp.
Herpestidae or Viverridae indet.
Carnivora indet.
<i>Hipparrion</i> aff. <i>sitifense</i>
<i>Stephanorinus africanus</i>
Suidae indet. cf. <i>Kolpochoerus afarensis</i>
<i>Hexaprotodon</i> ?/ <i>Archaeopotamus hippoensis</i> cf. <i>Sivatherium hindeyi</i> / <i>maurusium</i>
<i>Taurotragus</i> cf. <i>gaudryi</i>
<i>Gazella</i> aff. <i>psolea</i>
<i>Parmularius</i> ? cf. <i>atlanticus</i>
Testudinidae cf. <i>T. hermanni</i> / <i>graeca</i>
<i>Centrochelys</i> purica
Fish remains
<i>Golunda aouraghei</i>
<i>Paraethomys pusillus</i>
<i>Paraethomys chikeri</i>
<i>Praomys</i> cf. <i>skouri</i>
<i>Irhoudia</i> sp.
<i>Atlantoxerus</i> sp.
<i>Eliomys</i> sp.
Gerbillidae indet.1
Gerbillidae indet.2
Alytidae vel Ranidae indet.
Lacertidae indet.
<i>Ophisaurus</i> sensu lato
Natricidae vel Elapidae indet.
Colubridae vel Lamprophiidae indet.

the associated fossil horizon were obtained from the combination of various methods including magnetostratigraphy, numerical dating and biochronology (Parés et al., 2023). The magnetostratigraphic study of the deposits led to the identification of a succession of 5 main intervals of normal (N1, N2 and N3, from bottom to top) and reverse polarity (R1 and R2). Guefaït-4 is positioned within N1 (Fig. 2). In parallel, numerical dating using ESR and U-series methods returned somewhat contrasting results. On the one hand, pre-screening of various fossil teeth of equids using Laser Ablation U-series analyses showed not only evidence of uranium leaching in the dentine, but also relatively high uranium concentration in the enamel, making the samples unsuitable for combined U-series/ESR dating (see details in Parés et al., 2023). On the other hand, ESR dating based on the Multiple Centre (MC) approach (Toyoda et al., 2000) and performed on optically-bleached quartz grains from the fossil horizon (ESR sample ID: 19GFS-E1) yielded ESR age estimates of 1.87 ± 0.31 Ma (1σ) and 1.68 ± 0.24 Ma (1σ) based on the measurement of the Aluminium (Al) and Ti signals (option D *sensu* Duval and Guilarte, 2015), respectively. In accordance with the principles of the MC approach and given the different bleaching rates of each signal (Duval et al., 2017), the ESR age result derived from the Ti signal was regarded as providing a closer estimate of the true burial age from a methodological perspective (Parés et al., 2023).

Importantly, the Al ESR age published by Parés et al. (2023) should be regarded as a maximum possible age, since the residual, unbleachable component of the signal could not be measured in due time, and was therefore initially not taken into account in the original study for the dose evaluation. A subsequent evaluation of the ESR intensity of the UV-bleached aliquot yielded an unusually low bleaching coefficient (expressed as the relative difference between the ESR intensities of the

natural and UV-bleached aliquots) of 28.6 %, leading to the subtraction of a massive residual component of the Al ESR signal (as per the principles of the based on the Total Bleach method; see Forman, 1989) and resulting in the calculation of a D_E value (EXP + LIN fitting with data weighting by $1/I^2$) of 1187 ± 184 Gy. This new dose estimate, which is significantly lower than the value of 3262 ± 513 Gy initially given by Parés et al. (2023), provides a revised Al ESR age of 0.68 ± 0.11 Ma. The reliability of this result as a chronological constraint for sample 19GFS-E1 may be reasonably questioned in the first instance, since a Middle Pleistocene age result appears to be strongly underestimated in comparison with the other lines of evidence available (i.e., magnetostratigraphy, biochronology and Ti ESR age result), which all point to a much older chronology. It should also be noted that the very low bleaching coefficient of 28.6 % measured for 19GFS-E1 is actually much lower than any values usually calculated for similar deposits in North Africa, which are systematically >45 % (e.g., Sahnouni et al., 2018; Bartz et al., 2018; Duval et al., 2023). This value is instead closer to those traditionally estimated from modern deposits (e.g., Voinchet et al., 2015), and may be therefore regarded as an additional indicator to reasonably question the accuracy of the Al ESR data obtained for 19GFS-E1. Possible explanations for this massive age underestimation will be further discussed later in the manuscript (subsection 4.1.).

In summary, Parés et al. (2023) initially proposed three alternatives for the correlation of the local magnetostratigraphy to the GPTS (see illustrative support in Supplementary Material Fig. S1) based on the data available at the time. Using the biochronological evidence pointing an age close to the Plio-Pleistocene boundary for the large mammal and rodent fossil assemblage from GFT-4 (see complete discussion in Parés et al., 2023), Option 1 correlates N1, N2 and N3 to the Gauss chron (3.60–2.61 Ma), Feni excursion (2.16 Ma) and Olduvai Subchron (1.93–1.78 Ma), respectively. In contrast, Option 2 supports the Ti ESR age result, which is compatible within error with a correlation of the magnetozone N1 hosting the fossil horizon to the Olduvai Subchron (1.93–1.78 Ma). In other words, Option 2 assumes younger chronologies by correlating N1, N2 and N3 to the Olduvai Subchron (1.93–1.78 Ma), Jaramillo Subchron (1.08–1.01 Ma) and Brunhes Chron (<0.77 Ma), respectively. Finally, option 3 is a mixture of the first two and proposes a correlation of N1, N2 and N3 to the Gauss chron (3.60–2.61 Ma), Olduvai Subchron (1.93–1.78 Ma) and Brunhes chron (<0.77 Ma), respectively. Importantly, with options 1 and 3 the fossil horizon Guefaït-4 is positioned within Gauss chron (3.60–2.61 Ma), whereas it is being correlated to Olduvai Subchron (1.93–1.78 Ma) in option 2. While the validity of each option has been extensively discussed in Parés et al. (2023) through lithostratigraphic, sedimentary, geomorphological and biostratigraphic/biochronological evidence, the authors initially favoured Option 1, providing thus a minimum age constraint of 2.61 Ma for Guefaït-4. No age estimation was tentatively provided by Parés et al. (2023) for the fossil horizon, although an age close to 2.61 Ma was initially assumed given its relative stratigraphic proximity to the magnetic reversal (a few meters) attributed to the Gauss-Matuyama transition.

3. Material and methods

3.1. Sampling

Sampling was performed by taking into account the minimum requirements and specificities of each dating method (e.g.: (i) minimum amount of pure quartz needed: a few g for ESR, >10 g for TCN; (ii) need to focus on low-radioactivity deposits for ESR; (iii) time range applicability of both methods). This is why we specifically targeted sandy, quartz-rich sediment layers located above and below the fossiliferous horizon in order to (i) ensure the combined application of both dating methods on a given layer and (ii) obtain minimum and maximum age constraints for GFT-4.

Consequently, a first sampling site was selected for both ESR

(22GAF-E1) and TCN (22GAF-TCN1) methods from a silty, fine-grained red sandstone positioned at a height of about 62 m in the composite section (Figs. 2 and 3), i.e. ~10 m below the upper limestone conglomerate with gastropods (Limestone C; Fig. 2). The second sampling site was chosen ~6 m above the Limestone C, in the upper part of a thin limestone conglomerate, with less abundant cobbles towards the top (+79 m in the composite section; Fig. 2). Importantly, these two sampling sites are positioned a few meters below (~5 m) and above (~11 m) the fossil horizon, respectively. Finally, a third sampling site was selected for TCN dating only (22GAF-TCN2) from a well-bedded red medium-grained, clayey sandstone layer from about 10 m below the massive conglomerate at the base of the sequence (i.e., at 22 m of the composite section; Fig. 2), in order to test the TCN method on the oldest deposits of the section.

3.2. ESR dating of quartz grains

Sample preparation and ESR dating procedures followed Parés et al. (2023). Unlike sampling site 1 (ESR sample ID: 22GAF-E1), the site 2 sample (ESR sample ID: 22GAF-E2) did not contain sufficient amounts of quartz for ESR, and inevitably nor for TCN dating, precluding thus any further analysis of this sample. The 100–200 µm quartz grain fraction of 22GAF-E1 was dated via a Multi-grain Multi-aliquot Additive dose method (MAAD) following the Multiple Centre approach (Toyoda et al., 2000). The sample was divided into 15 aliquots of ~150 mg each: one was UV-bleached for about 1500 h using a SOL2 solar simulator, thirteen were gamma irradiated from 42.8 Gy to 18.8 kGy (see detailed irradiation dose steps in Fig. 4) using a Gammacell-1000 Cs-137 source, while a last one was kept untouched (=natural aliquot).

ESR measurements were performed at low temperature (~92 K) using a Bruker EMXmicro X-band ESR spectrometer (see Setup 1 in Guijarro and Duval, 2021). The radiation-induced ESR signals of the Aluminium (Al) and Ti signals were acquired together in a single spectrum (see experimental conditions in Fig. 4), and ESR intensities were measured following Toyoda and Falguères (2003) and option D *sensu* Duval and Guijarro (2015), respectively (Fig. 4A), after a baseline correction performed with a cubic function with Bruker WINEPR software. Option D results from a mixture of contributions from Ti-H and Ti-Li lines, and may be regarded as a proxy for the ‘total Ti concentration’ initially defined by Beerten and Stesmans (2006a) as the most reliable option for ESR dating based on the Ti signal beyond the late Middle Pleistocene. In particular, the potential of Option D evaluation for providing reliable and accurate chronological constraints to Early-to-Middle Pleistocene quartz samples has been demonstrated by a series of multi-technique dating studies in which ESR provided consistent results with the independent age control (e.g., Voinchet et al., 2020;

Duval et al., 2022, 2023, 2024a; Bartz et al., 2018, 2019a). All aliquots were measured 3 times after a ~120° rotation in the cavity in order to compensate for the angular dependence of the Al and Ti signals caused by sample heterogeneity. These measurements were then repeated three over distinct days in order to evaluate the variability of ESR data (Duval et al., 2024b).

For each aliquot, ESR intensities of Al and Ti centres were corrected by the corresponding number of scans, aliquot mass and a temperature correction factor (Duval and Guijarro, 2015). Additionally, the residual, unbleachable ESR intensity of the Al signal estimated from the UV-bleached aliquot was subtracted from the ESR intensities of all aliquots, following the usual Total Bleach method (Forman, 1989; Voinchet et al., 2003). Final Dose Response Curves (DRCs) were obtained by using the mean normalised ESR intensities and associated error (1 standard deviation) derived from the repeated measurements (Fig. 4B and C).

For the Al signal, dose response curve (DRC) fitting was carried out with an Exponential plus Linear (EXP + LIN) function following Duval (2012). This function may approximate the behaviour of the signal with the dose, which is known to follow a Double Saturating Exponential (DSE) function (Benzid and Timar-Gabor, 2020), when only a limited maximum applied dose (D_{\max}) is employed (i.e., <20 kGy here). For the Ti signal, two fitting functions were employed: (i) the Ti-2 function, a two-component function made of the combination of a standard SSE and a negative SSE, over the full dose range ($D_{\max} = 18.8$ kGy) in order to properly describe the non-monotonic behaviour of the signal, and especially the radiation bleaching at high doses (e.g., Woda and Wagner (2007) usually observed above 10 kGy (Duval and Guijarro, 2015); (ii) a SSE function until selected D_{\max} values. A combination of fitting options involving equal weights (EW) and data weighting by the inverse of the square intensity ($1/I^2$) or by the inverse of the square experimental error ($1/s^2$) was considered in order to evaluate any potential fitting bias (Fig. 4 and Table 2).

The dose rate was evaluated through a combination of field and laboratory measurements. Gamma dose rate was measured in situ at the exact sampling spot using a Canberra-Mirion NaI probe connected to an Osprey multichannel analyser and evaluated through the Threshold method (Duval and Arnold, 2013), with additional corrections following Martin et al. (2024). External alpha and beta dose rate components were calculated from the radioelement concentrations of the raw sediment measured by ICP-MS/OES following a four-acid digestion procedure. Dose rate calculations (Table 3) were performed with DRAC (v1.2.) (Durcan et al., 2015), using the dose rate conversion factors from Guérin et al. (2011), alpha attenuation from Brennan et al. (1991), beta attenuations from Guérin et al. (2012) and etching depth attenuations from Brennan (2003). Etching depths values of 10 ± 5 µm were considered



Fig. 3. Sediment samples collected from sites 1 and 3 for ESR (blue) and TCN (red) dating methods. Left: Samples 22GAF-E1 (ESR) and 22GAF-TCN1 (TCN), collected from the same level (sampling site 1; see stratigraphic position in Fig. 2); Right: Sample 22GAF-TCN2 (sampling site 3; see stratigraphic position in Fig. 2). Note that sampling site 2 is not shown, as it did not yield a sufficient amount of quartz for ESR and TCN dating (see text). (For interpretation of the references to colour in this figure legend, the reader is referred to the Web version of this article.)

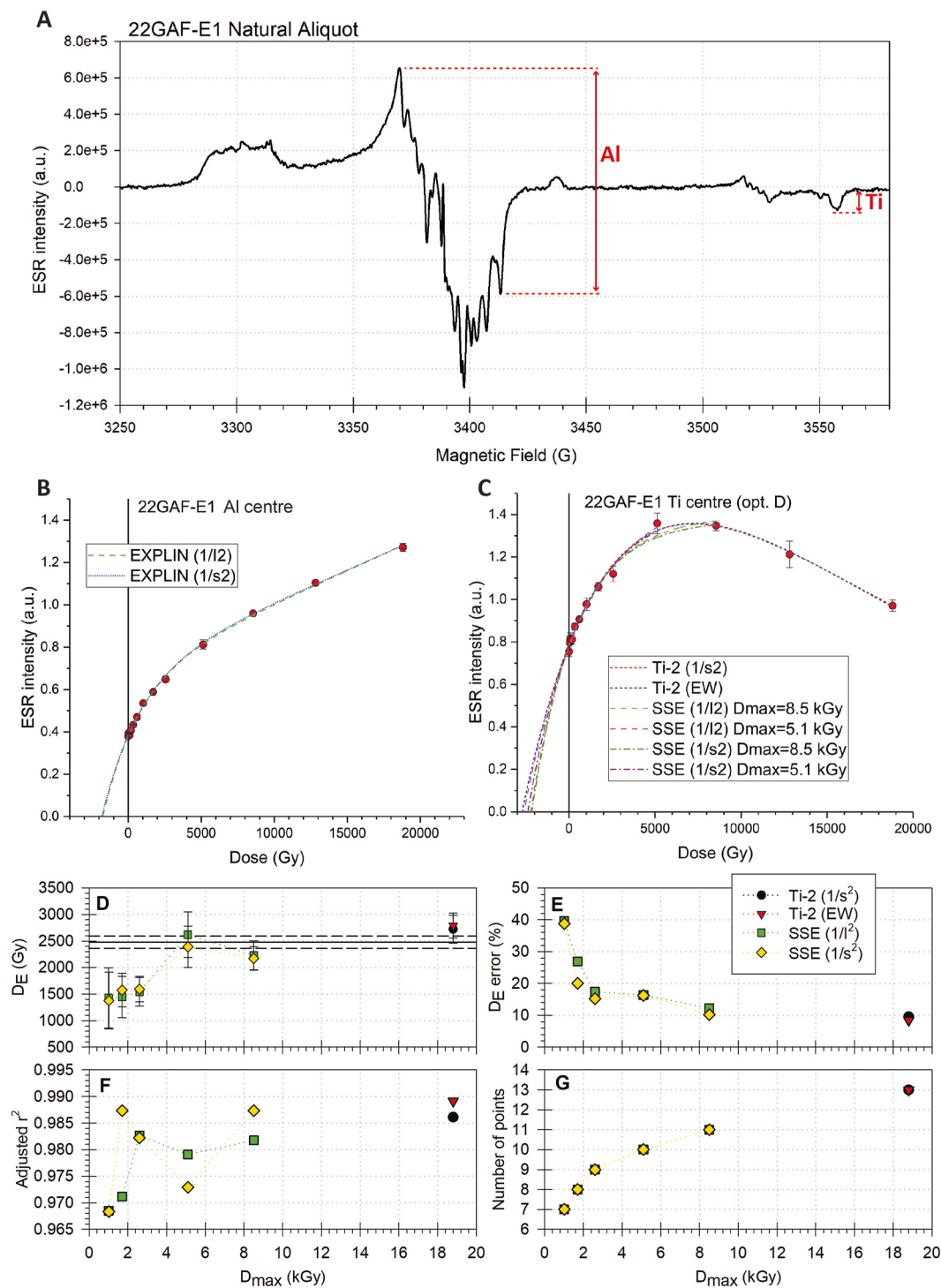


Fig. 4. Graphical display of the ESR data obtained for sample 22GAF-E1. (A): Example of ESR spectrum (natural aliquot). ESR measurements were performed using the following acquisition parameters: 5 mW microwave power, 1024 points resolution, 35 mT sweep width, 100 kHz modulation frequency, 0.1 mT modulation amplitude, 60 ms conversion time, 10 ms time constant and 1–3 accumulated scans depending on the aliquot considered. B and C: Dose Response Curves of the Al and Ti signals measured in sample 22GAF-E1. Irradiation dose steps are: 0, 42.8, 85.5, 171.1, 342.0, 598.4, 1025.8, 1709.7, 2564.5, 5129.1, 8548.4, 12822.7 and 18806.6 Gy. . D, E, F and G: fitting sensitivity tests for the ESR DRCs of the Ti signal evaluating the influence of D_{max} on the D_E values (D), relative D_E error (E), adjusted r² values (F) and number of points considered in the DRC (G). The corresponding numerical values may be found in [Supplementary Material Table S1](#). For the ESR age calculation, a weighted mean D_E value was derived from the D_E value corresponding to D_{max} > 4 kGy (cluster #2; see text for explanation).

following Duval et al. (2018). Current water content was evaluated in the laboratory by drying the sediment at 50 °C in an oven during three weeks, returning an almost dry value of 1.1 %. The saturated water content was experimentally evaluated to 57 %. Importantly, note that water contents are expressed in % dry weight throughout the manuscript

(as required by DRAC), and not in % wet weight as it is usually the case within the ESR dating community (e.g., Grün, 1994). A large absolute associated error of ±10 % was used for the long-term water content in order to encompass for any significant variation of water content throughout time. Internal dose rate was assumed to be 30 ± 10 µGy/a,

based on the work from Vandenberghe et al. (2008) and using an alpha efficiency of 0.07 ± 0.01 (Bartz et al., 2019b). Cosmic dose rate was calculated using Prescott and Hutton (1994) and using the depth below the top of the composite section (70 m) as the most reliable estimate of the long-term depth. A significant associated error of ± 5 m was considered. All errors are 1σ .

3.3. TCN burial dating

TCN dating, more specifically the TCN burial dating based on beryllium-10 (^{10}Be) and aluminum-26 (^{26}Al) measured in quartz, utilizes the differential decay of the two nuclides and its offset from the assumed nominal surface production ratio (e.g., Granger and Muzikar, 2001; Granger, 2014; Rixhon, 2023). It has been applied in various settings in geomorphology for the last couple of decades (e.g., Granger et al., 1997; Balco et al., 2005; Fujioka et al., 2009; Rixhon, 2020;

Table 2

ESR data collected from the measurement of the Al and Ti signals measured in sample 22GAF-E1.

	Sample	22GAF-E1
Al signal	Average aliquot weight (mg)	150.4 ± 0.2
	Repeated measurements	3
	S/N ^a	116
	Mean ESR intensity precision ^b (%)	1.2
	D _E precision ^c (%)	3.5
	Bleaching coef. (%) ^d	51.6 ± 0.9
	EXPLIN (1/ I^2) fitting	
	Adjusted r ²	0.997
	D _E (Gy)	1734 ± 158
	EXPLIN (1/ s^2) fitting	
Ti signal (Option D)	Adjusted r ²	0.998
	D _E (Gy)	1802 ± 119
	Weighted mean	
	D _E (Gy)	1777 ± 95
	S/N ^a	10.7
	Mean ESR intensity precision ^b (%)	0.3
	D _E precision ^c (%)	18.5
	Ti2 (1/ s^2) fitting [$D_{\max} = 18.8$ kGy]: (i) data weighting 1/ s^2 /(ii) EW	
	Adjusted r ²	(i) 0.986/(ii) 0.989
	D _E (Gy)	(i) 2721 ± 260 /(ii) 2792 ± 235
Intensity ratios ^f	SSE (1/ I^2) fitting: (i) $D_{\max} = 8.5$ kGy/(ii) $D_{\max} = 5.1$ kGy	
	Adjusted r ²	(i) 0.982/(ii) 0.979
	D _E (Gy)	(i) 2231 ± 274 /(ii) 2620 ± 429
	SSE (1/ s^2) fitting: (i) $D_{\max} = 8.5$ kGy/(ii) $D_{\max} = 5.1$ kGy	
	Adjusted r ²	(i) 0.987/(ii) 0.973
	D _E (Gy)	(i) 2171 ± 222 /(ii) 2391 ± 389
	Weighted mean	
	D _E (Gy)	2477 ± 113
	Al/Ti(C) ^e	30.2
	Al/Ti(D)	10.9
	Ti(C)/Ti(D) ^e	0.37

^a The signal-to-noise (S/N) ratio was calculated from the first measurement of the natural aliquot. The noise intensity was measured from a field domain (>3570 G; see Fig. 4) displaying no interfering signal.

^b Relative variation (1 standard deviation) of the average ESR intensity over the repeated measurements (Duval et al., 2024b).

^c Relative variation (1 standard deviation) of the D_E values over the repeated measurements (Duval et al., 2024b). Fitting performed with the EXPLIN function with data weighting by 1/ I^2 and without subtracting the residual, non-bleachable, ESR intensity.

^d Bleaching coefficient is expressed as the relative difference between the ESR intensity of the natural and UV-bleached aliquots.

^e Ti(C) corresponds to the Ti-H signal option C *sensu* (Duval and Guilarte, 2015).

^f Intensity ratios were measured on the spectrum of the natural aliquot.

Table 3

Data inputs and outputs associated to the ESR age calculations. Errors are 1σ .

Sample	22GAF-E1
Current Depth (m)	70 ± 5
Current water content (% dry weight)	1.1
U (ppm)	1.10 ± 0.08
Th (ppm)	2.32 ± 0.11
K (%)	0.40 ± 0.02
Laboratory Gamma dose rate ($\mu\text{Gy/a}$) ^a	325 ± 31
Field Gamma dose rate ($\mu\text{Gy/a}$) ^b	710 ± 27
Laboratory: Field ratio	0.46
<i>ESR age calculation (long-term water content = 34 ± 10 %)</i>	
Internal dose rate ($\mu\text{Gy/a}$)	30 ± 10
Alpha dose rate ($\mu\text{Gy/a}$)	10 ± 5
Beta dose rate ($\mu\text{Gy/a}$)	346 ± 21
Gamma dose rate ($\mu\text{Gy/a}$)	511 ± 29
Cosmic dose rate ($\mu\text{Gy/a}$)	3 ± 0
Total dose rate ($\mu\text{Gy/a}$)	901 ± 37
Al D _E (Gy) ^c	1777 ± 103
Ti D _E (Gy) ^c	2477 ± 126
Al ESR age (Ma)	1.972 ± 0.171
Ti ESR age (Ma)	2.749 ± 0.226

^a Using the measured water content and dose rate conversion factors from Guérin et al. (2011).

^b As measured in the field.

^c In comparison with the values given in Table 2, final D_E errors include an additional 2.3 % uncertainty on the dose rate of the gamma irradiation source.

Malcrez et al., 2024) and has increasingly been applied in archaeological and paleoanthropological contexts over the recent years (e.g., Partridge et al., 2003; Pappu et al., 2011; Granger et al., 2015; Lebatard et al., 2019; Matmon et al., 2024).

In this study, two samples (22GAF-TCN1 and 22GAF-TCN2 from sampling sites 1 and 3, respectively; Table 4) were analysed for cosmogenic ^{10}Be and ^{26}Al concentrations to calculate burial ages. The samples were processed following a procedure established at CENIEH that was modified from previous studies (Kohl and Nishiizumi, 1992; Fujioka et al., 2015, 2022). Briefly, sediments were sieved into 75–500 μm grain size and treated via aqua regia to remove carbonates and iron oxides, heavy-liquid density separation, and three cycles of dilute hydrofluoric-acid (HF) etching to obtain pure quartz. Approximately 9–12 g of the purified quartz were spiked with ~ 0.21 mg ^{9}Be carrier (in the form of solution prepared from deep-mine beryl) and completely digested in concentrated (48 % w/w) HF. Small aliquots (~ 2 % volume of the quartz-dissolved solutions) were put aside for elemental aluminium measurement via in-house Inductively Coupled Plasma - Optical Emission Spectroscopy (ICP-OES) at CENIEH. Beryllium and aluminium were isolated from other unwanted elements (e.g., iron, titanium, boron) through anion and cation exchange chromatographies. Beryllium and aluminium hydroxides were precipitated with high purity $\text{NH}_3(\text{aq})$ and sent to the DREsden Accelerator Mass Spectrometry facility (DREAMS), Helmholtz-Zentrum Dresden-Rossendorf, Dresden, Germany, for the final treatment. The hydroxides were calcined to oxides and pressed into copper cathode sample holders after being mixed with niobium (Nb) powder for beryllium-oxide (BeO) samples (at the mass ratio of BeO:Nb = 1:4) and silver (Ag) powder for aluminium-oxide (Al_2O_3) samples (at the mass ratio of $\text{Al}_2\text{O}_3:\text{Ag} = 1:1$). $^{10}\text{Be}/^{9}\text{Be}$ and $^{26}\text{Al}/^{27}\text{Al}$ ratios were then measured at DREAMS (Rugel et al., 2016). Experimental parameters (including standards used for normalisation, procedural blanks and error propagation) are detailed in footnote in Table 4. ^{10}Be and ^{26}Al concentrations were calculated from the measured ratios after the standard normalisation and blank corrections (Table 4).

Burial ages were calculated following Granger (2014) and Granger and Muzikar (2001). The method assumes a simple exposure-burial scenario, where quartz particles exposed to cosmic rays at the steadily-eroding surface are later buried instantaneously. When the quartz particles are buried sufficiently deep and shielded from

Table 4Results of ^{10}Be and ^{26}Al measurements for TCN dating.

Sample ID	Latitude ($^{\circ}\text{N}$)	Longitude ($^{\circ}\text{W}$)	Elevation (m)	Depth (m)	$^{10}\text{Be}^{\text{a,c,d}}$ (10^4 atoms/g)	$^{26}\text{Al}^{\text{b,c,d}}$ (10^4 atoms/g)	$^{26}\text{Al}/^{10}\text{Be}$	Burial age ^e (Ma)
22GAF-TCN1	34.2179	2.4036	865	68	3.98 ± 0.31	5.3 ± 1.1	1.33 ± 0.30	3.35 ± 0.51 (0.59)
22GAF-TCN2	34.2201	2.4011	823	110	1.92 ± 0.15	10.3 ± 1.5	5.40 ± 0.87	0.50 ± 0.36 (0.36)

Errors denote one sigma.

^a Normalised to the standard SMD-Be-12 with the nominal $^{10}\text{Be}/^{9}\text{Be}$ ratio of $1.704 \pm 0.030 \times 10^{-12}$, which is traceable to NIST SRM4325 standard with the nominal ratio of $2.79 \pm 0.03 \times 10^{-11}$ (Nishiizumi et al., 2007; Akhmadaliev et al., 2013; Lachner et al., 2023).

^b Normalised to the standard SMD-Al-11 with the nominal $^{26}\text{Al}/^{27}\text{Al}$ ratio of $9.66 \pm 0.14 \times 10^{-12}$ (Merchel and Bremser, 2004; Rugel et al., 2016).

^c Corrected for procedural blanks with the average $^{10}\text{Be}/^{9}\text{Be}$ ratio of $3.2 \pm 0.4 \times 10^{-15}$ ($n = 2$) and $^{26}\text{Al}/^{27}\text{Al}$ ratio of $1.3 \pm 0.5 \times 10^{-15}$, which were 12–17 % and 4–7 % of the measured sample ratios, respectively.

^d Errors include in quadrature, AMS uncertainties (counting statistics, standard reproducibility, error in the standard nominal ratio, blank correction) and, for ^{10}Be , 1 % error from ^{9}Be concentration in the spike, whereas, for ^{26}Al , 3 % error from Al measurement via ICP-OES.

^e Calculated by following Granger and Muzikar (2001) and Granger (2014) using half-life values, 1.387 ± 0.012 Ma for ^{10}Be (Korschinek et al., 2010; Chmeleff et al., 2010) and 0.705 ± 0.024 Ma for ^{26}Al (Norris et al., 1983), assuming no prior-burial and no post-depositional production. Errors are ‘internal errors’ which include only analytical uncertainties associated with nuclide measurements, whereas errors in parentheses are ‘external errors’ which include analytical and systematic errors associated with nuclide production rates and half-lives. The latter errors must be used when these ages are compared with other dating methods.

cosmic-ray flux, $^{26}\text{Al}/^{10}\text{Be}$ ratios in the quartz will decrease as ^{26}Al decays faster (half-life, $t_{1/2} = 0.705 \pm 0.024$ Ma; Norris et al., 1983) than ^{10}Be ($t_{1/2} = 1.387 \pm 0.012$ Ma; Korschinek et al., 2010; Chmeleff et al., 2010), which can be used as a burial clock. The calculated burial ages in this manner are interpreted as either minimum or maximum ages. When burial depth is not sufficiently deep to shield cosmic-ray flux, nuclide productions will continue after burial, which counteracts the radioactive decay-based burial clock and leads to underestimation of burial time (i.e., the calculated age must be considered as a minimum estimate; Granger, 2014). In contrast, when the measured quartz particles had experienced prolonged periods of complete burial (a few hundred thousand years or more) before the current deposition, the burial clock will record the pre-historic burial time, and therefore the burial age calculated under the simple scenario described above will be overestimated (i.e., the calculated age must be regarded as a maximum estimate; Granger, 2014).

4. Results

4.1. ESR dating

4.1.1. ESR dose evaluation

ESR measurements of the Al signal show a repeatability that is higher than usual standards (Duval et al., 2024b), with a very limited variability of the mean ESR intensity (1.2 %) and of the D_E values (3.5 %) (Table 2). The bleaching coefficient of 51.6 % (Table 2) is within the range of values estimated elsewhere in the Moulouya basin (47–57 %; Bartz et al., 2018), suggesting thus similar bleaching and transport conditions. EXPLIN fittings carried out with data weighting by $1/I^2$ and $1/s^2$ return very close dose estimates of 1734 ± 158 and 1802 ± 119 Gy, indicating that there is no significant bias induced by the fitting procedure (Fig. 4B). A weighted mean D_E value of 1777 ± 95 Gy may therefore be proposed for the Al signal.

In comparison, ESR measurements of the Ti signals show a repeatability that is slightly below usual standards (Duval et al., 2024b), with a D_E scatter of 18.5 % despite the low variability of the mean ESR intensities (0.3 %) (Table 2). In order to evaluate any potential bias induced by the fitting, we carried out a series of sensitivity tests using a Ti-2 fitting function with equal weights and data weighting by $1/s^2$, and a SSE function with data weighting by $1/I^2$ and $1/s^2$ with a D_{\max} ranging from 1.0 to 8.5 kGy. Results are graphically displayed in Fig. 4D–G, while the corresponding numerical values are given in Supplementary Material Table S1 for completeness. The resulting dose estimates spread in two main clusters (Fig. 4D): (i) below 2000 Gy for $D_{\max} < 4$ kGy, (ii) and around 2500 Gy for $D_{\max} > 4$ kGy. Importantly, the first one overall shows much larger associated errors, systematically >15 % (28.6 % on average; Fig. 4E), and lower goodness-of-fit (average adjusted $r^2 = 0.976$; Fig. 4F), two criteria indicating a lower reliability of the fitting

results (Duval, 2012; Duval et al., 2013). Moreover, with only 7 to 9 experimental points considered (Fig. 4G), the SSE fittings related to the first cluster hardly meet the minimum requirements of 8–10 experimental points per DRC, with 3–4 points per fitted parameters, proposed by Lyons et al. (1992) to ensure a reliable fitting. In contrast, cluster #2 results show higher goodness-of-fit (average adjusted $r^2 = 0.983$; Fig. 4F), smaller relative D_E errors (12.2 % on average) and are based on DRCs using 10 to 13 experimental points, overall indicating higher reliability. Moreover, Fig. 4D show a correlation of D_{\max} and D_E values for D_{\max} from 1.0 to 5.1 kGy. This trend is usually be regarded as an indication of the inappropriateness of the fitting function to properly describe the behaviour of a given signal (e.g. Duval et al., 2009), indicating that accuracy of the D_E results should be treated with caution. In contrast, between $D_{\max} = 5.1$ kGy and $D_{\max} = 18.8$ kGy, D_E values reach a plateau around 2500 Gy, demonstrating that the D_{\max} has no longer a significant impact on the D_E . In other words, despite different fitting conditions, the D_E values remain within close range. To sum up, the dose estimates from cluster #2 show not only higher reliability but also higher accuracy. The use of two different fitting functions (Ti-2 and SSE) and three different data weighting options (EW, $1/s^2$, $1/I^2$) provides D_E estimates ranging from 2171 ± 222 Gy to 2721 ± 260 Gy. This variability illustrate the existing uncertainty on the fitting results, and since there are no objective methodological criteria to discard any of these results, a weighted mean D_E value of 2477 ± 113 Gy may therefore be proposed for the Ti signal.

The comparison of the D_E values following the MC approach shows that the Al signal returns a significantly lower value than the Ti signal, which is quite unusual since the Al signal tends to provide either a similar or higher dose estimate given its much slower bleaching kinetics (see basic principles of the MC approach in Toyoda et al., 2000; Duval et al., 2017). In other words, this D_E pattern cannot be explained by an incomplete reset of the Ti signal: the hypothesis that the Al signal has achieved a higher level of optical bleaching than the Ti signal can simply not be supported by our current knowledge and understanding of these radiation-induced ESR signals, since Ti signals are known to reset much faster than the Al signal (e.g., Toyoda et al., 2000; Tissoux et al., 2007; Duval et al., 2017). This result will be further discussed in section 5.1.2.

4.1.2. Dose rate evaluation

The main sources of uncertainty on the dose rate evaluation are typically the following: (i) long-term depth, (ii) spatial heterogeneity of the surrounding environment, and (iii) long-term water content.

First, the uncertainty on the cosmic dose rate as the result of an inaccurate estimation of the long-term depth is most likely minimum here: given the current depth below the top of the section (>50 m), the cosmic dose rate is negligible for 22GAF-E1 (3 $\mu\text{Gy/a}$; Table 3) and carry very little weight in the total dose rate (<0.5 %). In the first instance, the current depth of the sample below the top of the composite section (70

m) may be reasonably regarded as the most reliable estimate of the long-term depth. While we cannot exclude that some deposits might have been eroded from the uppermost part of the section, the uncertainty on the dose rate is minimum here: an increased overburden thickness would result in larger depth values, thus reducing even more the cosmic dose rate, which is already almost negligible in the total dose rate.

In order to evaluate the heterogeneity of the sedimentary environment, the natural radioactivity of the sediment was evaluated in situ and in the laboratory. Interestingly, the raw sediment collected from the sampling spot and closely associated to 22GAF-E1 shows relatively low natural radioactivity, as documented by the radioelement concentrations ($U = 1.10 \text{ ppm}$; $\text{Th} = 2.32 \text{ ppm}$; $K = 0.40 \%$; [Table 3](#)): they correspond to a gamma dose rate of $325 \pm 30 \mu\text{Gy/a}$ when using the measured water content. This value is $>50 \%$ lower than the gamma dose rate measured in the field ($710 \pm 27 \mu\text{Gy/a}$) at the sampling spot. The latter naturally accounts for the heterogeneity of the surrounding environment within a 30–40 cm radius sphere around the sample. In other words, these results indicate that the surrounding deposits show a much higher radioactivity than the sediment being dated. Since these deposits effectively contribute to the gamma dose rate absorbed by 22GAF-E1, they must therefore be taken into account in the dose rate evaluation. If not, considering a laboratory-derived gamma rate would induce a significant underestimation of the total dose area by $\sim 30 \%$, and lead to an ESR age overestimation of the same magnitude. To sum up, these results illustrate the importance of carrying out field measurements in heterogeneous sedimentary environments.

The evaluation of the long-term water content is challenging, especially over such a long time period. This value should be a time-averaged estimate of the water content over the burial period. In this context, the current and saturated water content values of 1.1 % and 57 % measured in the laboratory may provide useful minimum and maximum constraints, respectively. However, none of them can be regarded as reliable estimates of the long-term water content, as they imply two extreme, and most unlikely scenarios considering that either totally dry or fully wet conditions have prevailed throughout the sediment burial history. A common assumption in trapped-charge dating is to regard the 60 % of the saturated water content as the most suitable estimate for the long-term water content (e.g., [Duval et al., 2024a](#); [Demuro et al., 2024](#) and references therein). Here, this would correspond to 34 % (equivalent to 25 % wet weight), which may be considered as a fair estimate of the long-term water content compatible with the geological evidence available. Indeed, Units 2 to 4 of the composite section, which stratigraphically overlie the ESR sample, show a dominantly lacustrine and palustrine depositional environment characterized by the recurrent presence of water through time ([Fig. 2](#); see also [Parés et al., 2023](#); [Ramírez-Pedraza et al., 2024](#)). This sedimentation phase was followed by a fluvial incision resulting from the more recent opening of the Oued Za basin and its connection to the Moulouya River catchment, which most likely induced a drop in the Oued Za base level, and may have eventually impacted the water content in sediment. However, the exact timing and duration of these two main phases as well as the magnitude of the associated water content remain largely unknown, making any further discussion quite speculative. In order to roughly evaluate that extent a progressive decrease of the water content would impact the time-averaged value, a series of very basic simulations involving different (and oversimplified) scenarios was carried out: assuming that a water content of 34 % has prevailed through most of the burial period (from 90 % to 50 %), followed by a progressive decrease to the current-day value (1.1 %), would result in time-averaged values of between 32.3 and 25.8 %, as illustrated by [Fig. 5](#). For example, a progressive decrease of the water content on the last 20 % of the burial period, would only induce a slight decrease ($<4 \%$) on the time-averaged water content, resulting a slightly higher total dose rate (+3 %) and a reduction of the ESR age by the same amount ([Table S2](#)). Importantly, these time-averaged water content values are systematically within the 1σ error range (24–44 %) considered for dating purpose, whatever the

scenario considered. To sum up, while we do acknowledge the existing intrinsic uncertainty on the evaluation of the long-term water content, the value of $34 \pm 10 \%$ considered in the present work is compatible with the geological evidence, while a recent drop in the water content would have only limited impact on the time-averaged value. Nevertheless, for completeness we do also provide the total dose rate values corresponding to the long-term water contents ranging from 1.1 to 57 % ([Table S2](#)).

4.1.3. ESR age calculation

Given the above, calculations were performed using a long-term water content of $34 \pm 10 \%$, long-term depth of $70 \pm 5 \text{ m}$ and a gamma dose rate derived from the in situ measurement: they return ESR age results of $1.97 \pm 0.17 \text{ Ma}$ and $2.75 \pm 0.23 \text{ Ma}$ for the Al and Ti signals, respectively. From a methodological perspective, we regard these results as the most reliable estimates that may be derived from the existing data set.

Additional sensitivity tests were nevertheless carried out in order to properly evaluate to what extent the two main sources of uncertainty identified earlier, related to the fitting of the Ti ESR data (section 3.1.1) and to the evaluation of the long-term water content (section 3.1.2.) may impact the calculated ages. First, the scatter of the various Ti D_E values belonging to data cluster #2, regarded as providing more reliable fitting results, yield ESR ages ranging from 2.41 ± 0.30 to $3.10 \pm 0.34 \text{ Ma}$ ([Supplementary Table S2](#)). These results differ by between -12% and $+13 \%$ from the age of $2.75 \pm 0.23 \text{ Ma}$ i.e., remaining in agreement within error with the initial calculation. In comparison, considering long-term water content of between 1.1 % (current water content) and 57 % (saturated water content), two extreme and unlikely scenarios, would lead to minimum and maximum ESR age results of 2.01 ± 0.12 and $3.26 \pm 0.25 \text{ Ma}$, respectively. In general, a $\pm 10 \%$ variation in the water content would result in a variation of the total dose rate, and of the ESR age, of about $\pm 7\text{--}9 \%$. More specifically, considering a slightly lower long-term water content of $30 \pm 10 \%$ (instead of the initial $34 \pm 10 \%$) would yield younger Al and Ti ESR ages by 3 %. A similar test using a long-term water content of $40 \pm 10 \%$ would produce ages older by 5 %. Regardless, all ESR ages remain within error. The main outcomes of our various sensitivity tests are fully displayed in [Supplementary Tables S1 and S2](#) for completeness.

4.2. TCN burial dating

Results of ^{10}Be and ^{26}Al measurements from the two samples, 22GAF-TCN1 and 22GAF-TCN2, are shown in [Table 4](#). Calcareous nature of the bulk materials and relatively fine grain size of quartz made difficult to extract pure quartz, resulting in low quartz-extraction efficiency (0.6–3 %) for these samples. Measured $^{10}\text{Be}/^{9}\text{Be}$ and $^{26}\text{Al}/^{27}\text{Al}$ ratios are also at low level, $\sim 2\text{--}3 \times 10^{-14}$, typically expected from long-buried samples, resulting in relatively high analytical uncertainties of 6–20 %. Calculated ^{10}Be concentrations are 1.9 and $4.0 \times 10^4 \text{ atoms/g}$ (Qz) with $\sim 8 \%$ errors, and ^{26}Al concentrations are 5.3 and $10.3 \times 10^4 \text{ atoms/g(Qz)}$ with 14–21 % errors, respectively. Burial ages were calculated assuming initial nuclide production at a steadily-eroding surface at a postulated sediment source location (latitude 34.3°N and elevation 1300 m) using the sea-level-high-latitude ^{10}Be production rate of 4.01 atoms/g/yr ([Borchers et al., 2016](#)) and ^{26}Al production rate of 27.07 atoms/g/yr (calculated assuming $^{26}\text{Al}/^{10}\text{Be}$ production rate ratio of 6.75; [Balco et al., 2008](#); [Borchers et al., 2016](#)) scaled by the time-independent [Lal \(1991\)](#)/[Stone \(2000\)](#) method. Assuming also no prior-burial before the current deposition and no post-depositional production, the model simple burial ages are calculated to be 3.35 ± 0.51 (0.59) Ma and 0.50 ± 0.36 (0.36) Ma for the samples 22GAF-TCN1 and 22GAF-TCN2, respectively. The smaller 1σ uncertainty includes only analytical errors (“internal” error), whereas the larger 1σ uncertainty in parentheses includes systematic errors from the half-lives and the production rates (“external” error). The latter is appropriate for

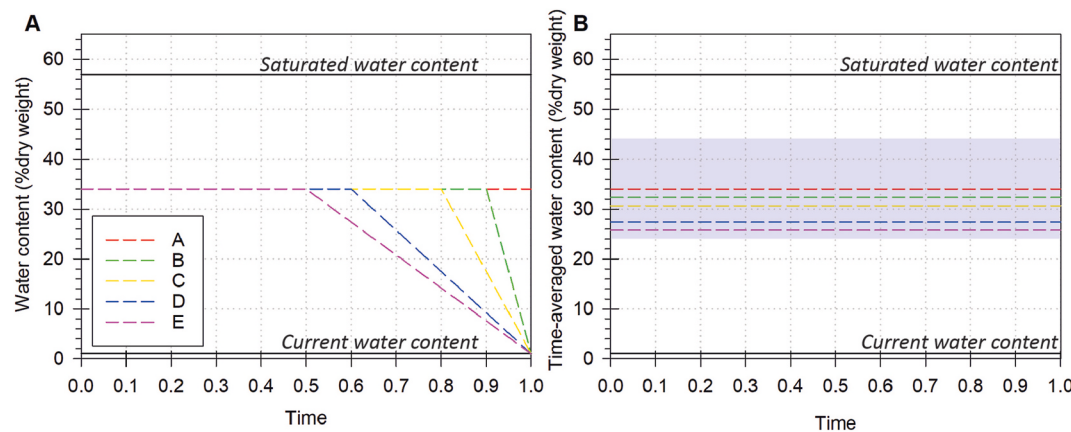


Fig. 5. Evolution of the water content through time (A) and the resulting time-averaged value (B). Time ranges from 0 (burial event) to 1 (today). Different scenarios (A to E) are considered, with a constant 34 % water content (=60 % of the saturated water content, a standard assumption in Luminescence and ESR dating; see text for explanations) during the whole burial history (A), or for 90 % of the burial history followed by a progressive decrease until the current-day value (B), or for 80 % (C), 60 % (D), 50 % (E) of the burial history. The corresponding time-averaged water content value falls systematically within the $34 \pm 10\%$ (grey band in Graph 5B), i.e. the range considered for dating purpose (see main text).

comparing with data from other dating methods (Table 4).

5. Discussion

5.1. Evaluating the reliability and accuracy of the numerical dating results

5.1.1. Summarising the chronological evidence available

The numerical age results available for Dhar Iroumyane section basically falls into three main groups. The first one includes the ESR sample 19GFS-E1 and TCN samples 22GAF-TCN2, which yielded Middle Pleistocene ages of 0.68 ± 0.11 Ma (Al signal) and 0.50 ± 0.36 Ma, respectively. The second group is made of ESR samples 19GFS-E1 and 22GAF-E1, with Early Pleistocene age estimates of 1.68 ± 0.24 Ma (Al signal) and 1.97 ± 0.17 Ma (Ti signal), respectively. Finally, the third group is composed by ESR sample 22GAF-E1 and TCN sample 22GAF-TCN2, which returned Late Pliocene ages of 2.75 ± 0.23 Ma (Ti signal) and 3.35 ± 0.59 Ma, respectively.

Importantly, the accuracy of these ESR and TCN dating results can be evaluated by comparison with the independent age control available from the paleomagnetism and biochronology. All the samples mentioned above are positioned within the N1 interval of the local magnetostratigraphy (Fig. 2), thus associated with a normal polarity. Consequently, a tentative correlation to the Geomagnetic Polarity Time Scale (GPTS) based on the numerical age results available would suggest that N1 could either be Brunhes (<0.77 Ma; Group #1), Olduvai Subchron (1.93–1.78 Ma; Group #2) or Gauss Chron (3.60–2.61 Ma; Group #3).

The latter is by far the most compatible with the magnetostratigraphic and biochronological evidence available, as already extensively pointed out by Parés et al. (2023), while the other two options raise a series of issues. For example, a correlation of N1 to Brunhes is in clear contradiction with not only the magnetostratigraphy showing other normal polarity intervals (N2 and N3) above N1, but also the biochronology and the known temporal range of most taxa largely restricted to the Early Pleistocene (see detailed discussion in Parés et al., 2023; Van der Made et al., 2021). Consequently, the age results of Group #1 may be regarded as strongly underestimated. In a similar way, a potential correlation of N1 to Olduvai Suchron (Group #2) has been already extensively discussed and regarded as very unlikely by Parés et al. (2023), mostly on biochronological grounds. As indicated by the authors (p. 30) “a correlation to the Olduvai chron would greatly extend the known temporal range of several taxa in North Africa, including the hippocions without ectostylids, but not of *Hipparrison* in general.”. Moreover, other issues strongly weaken the likeliness of a correlation of

N1 to the Olduvai Subchron, as emphasized by Parés et al. (2023): (i) the apparent thickness N1 (>75 m), which would imply a massive sediment accumulation rate (SAR) of at least 50 cm/ka (the lower reversal has not been identified in the section; see Fig. 2); (ii) the presence of two unknown magnetic excursions within N1 Olduvai (see Fig. 2, at heights of 28 and 31 m within N1), which cannot be related to any known excursions within Olduvai (see Ogg, 2020).

In summary, we may reasonably conclude that age results belonging to Groups #1 and #2 may be regarded as underestimated, while those of Group #3 are instead compatible with the various independent lines of evidence available, providing additional support to the conclusions of Parés et al. (2023). This is the most parsimonious interpretation of the existing chronological data set. The potential causes for these age underestimations are further discussed below from a methodological perspective.

5.1.2. ESR dating

5.1.2.1. The unusual D_E pattern. Like ESR sample 19GFS-E1 initially published by Parés et al. (2023), 22GAF-E1 also shows this unusual D_E and age pattern with the Ti signal providing higher dose estimates and older age results than the Al signal, which in turn systematically returns underestimated ESR ages (see section 5.1.1). To our knowledge, this is the first time that such an age pattern is reported with a clear evidence of the Al signal providing an age underestimation.

First, such an underestimation resulting from a saturation of the radiation-induced ESR signal is in the first instance quite unlikely, because not supported by the ESR DRCs of the Al signal measured in both samples (Fig. 4; see also Fig. 10 in Parés et al., 2023). Actually, the Al signal usually does not show apparent saturation at high doses, even when exceeding several tens of kGy (e.g., Lin et al., 2006; Duval, 2012; Benzid and Timar-Gabor, 2020). Additionally, the magnitude of the Al D_E values obtained on these two samples after bleaching is not especially high (<2000 Gy), but is rather within the usual range of 1000–2500 Gy typically measured for North African Cenozoic sediment samples >1 Ma (e.g., Sahnouni et al., 2018; Bartz et al., 2018; Duval et al., 2023).

Second, the possibility of a lower thermal stability of the Al signal may not be reasonably excluded. The literature available remains very contrasted in that regard, with previous works showing either a higher thermal stability of the Al signal compared to the Ti signal (e.g., Toyoda and Ikeya, 1991), or the opposite (Toyoda and Ikeya, 1994; Wen et al., 2024), leading Toyoda (2015) to conclude that this may be strongly sample dependent. Consequently, given the long time range considered here (>2.6 Ma) we cannot not reasonably exclude that the lower dose

estimates given by the Al signal might be resulting from a comparatively lower thermal stability, although additional experimental data will be required in the future in order to confirm this hypothesis.

5.1.2.2. What makes 22GAF-E1 and 19GFS-E1 different? ESR samples 22GAF-E1 and 19GFS-E1 return significantly different (but stratigraphically-consistent) Ti ESR age estimates of 2.75 ± 0.23 Ma and 1.68 ± 0.24 Ma, respectively. Importantly, despite the existing uncertainty on the DRC fitting and the long term water content, our various sensitivity tests (*Supplementary Tables S1 and S2*) carried out on sample 22GAF-E1 systematically return a much older Ti ESR age result compared to 19GFS-E1. In particular, when considering the uncertainty on the long-term water content alone (i.e., without factoring in the fitting uncertainty), and a water content as low as $20 \pm 10\%$ (=17 % wet weight; i.e., similar to that initially assumed by Parés et al., 2023), it may be observed that the Ti ESR age remains in agreement within 1σ error (2.44 ± 0.22 Ma; *Supplementary Table S2*) with a Gauss chronology (>2.61 Ma). 22GAF-E1 being located below 19GFS-E1 by ~ 5 m, we cannot exclude that part of age difference may be simply due to their respective stratigraphic position, potentially amplified by the presence of a sedimentary hiatus or a significant change in sediment accumulation rate between Units 1 and 2. However, this unlikely fully explains the magnitude of the age gap and why the age of 19GFS-E1 is strongly underestimated (by ~ 1 Ma), and we explore below the possible influence of other sources of uncertainty, including (i) the composition of the Ti ESR signal, (ii) the ESR data processing and (iii) the depositional environment.

First, this age discrepancy between the two samples cannot be explained by different ESR signal characteristics, since they both show similar C/D signal intensity ratios of 0.37–0.38 for the natural aliquot (**Table 3**), indicating similar relative contributions of Ti-H and Ti-Li lines to the ESR intensity measured through option D (see also Demuro et al., 2020). In other words, while the limitations of the Ti-H signal to provide accurate dose estimates beyond several hundreds of Gy have been widely documented (e.g. Bartz et al., 2020; Voinchet et al., 2020, Xu et al., 2024), here we cannot relate the younger age of 19GFS-E1 to a higher proportion of Ti-H signal in the sample. As an aside observation, we notice that this C/D ratio is lower than those obtained for other (Early Pleistocene) quartz samples from the Moulouya River (0.41–0.56; Bartz et al., 2018), i.e. from within the same river catchment area. This difference might be related to quartz of distinct nature (and origin), although a dose effect may not be excluded. The C/D ratio is also lower than the average value of 0.45 ± 0.05 calculated from a range of Pleistocene samples of different origins published earlier by Duval and Guilarte (2015) and those reported by Xu et al. (2024) (0.67–0.84). This may be tentatively explained by the much older age of the two samples from Guefait-4, implying thus a reduced influence of the less stable Ti-H signal (see Duval and Guilarte (2015) and Bartz et al. (2020) on this matter).

Unlike in the present study, no baseline correction was initially applied to the ESR spectra collected for sample 19GFS-E1 initially published by Parés et al. (2023). Consequently, the original data set was reprocessed and a new D_E value of 2870 ± 349 Gy (Ti-2 fitting with data weighting by $1/s^2$) was obtained after baseline correction. This estimate is only $\sim 2\%$ lower than the value initially published (2935 ± 402 Gy), demonstrating the high robustness of the ESR data set. In other words, ESR data processing has negligible impact on the age difference observed between the two samples.

Finally, the sedimentary context, in the broad sense, may also possibly explain these differences. While sample 19GFS-E1 yields a dose estimate that is ~ 400 Gy higher than that of 22GAF-E1, the resulting age is significantly younger by ~ 1.0 Ma. Consequently, the age scatter observed between the samples is most likely related to the corresponding environmental dose rates, which significantly differ by ~ 700 μ Gy/a (1745 ± 81 μ Gy/a vs. 1017 ± 73 μ Gy/a). 19GFS-E1 was initially

collected from clayey siltstones showing a much higher natural radioactivity compared to that of 22GAF-E1, which originates from coarser deposits (U: 1.82 ± 1.10 ppm; Th: 5.89 ± 2.32 ppm; K: 1.24 ± 0.40 %). It is probably no coincidence that the sample providing an older age result (22GAF-E1), consistent with the independent age control, originates from an environment showing a significantly lower dose rate. While a D_E value of about 4900 Gy should theoretically be obtained for 19GFS-E1 to obtain an age of ~ 2.8 Ma similar to that of 22GAF-E1, the D_E of 2935 ± 402 Gy experimentally obtained does provide an indirect indication of the maximum dose that could be accurately estimated from the Ti signal, which may be defined as the upper limit of dose quantification (ULDQ). In other words, following a similar reasoning that led other authors to conclude earlier that the Ti-H signal would provide underestimated ages for D_E values above 300–400 Gy (e.g., Voinchet et al., 2020; Bartz et al., 2020; Duval et al., 2023), or higher (Xu et al., 2024), we hypothesize here that the Ti signal can provide accurate dose estimates of the true burial dose up to a maximum of ~ 3000 Gy. While we do acknowledge the need for future investigations to confirm or refute this working hypothesis, it can nevertheless be observed that previous ESR dating studies of ≥ 1.8 Ma quartz samples providing consistent results with the independent age control available have all in common the calculation of a D_E value < 3000 Gy (e.g., Rink et al., 2007; Sahnouni et al., 2018; Duval et al., 2023). These results indirectly show the importance of targeting especially low-radioactivity deposits when dealing with samples whose burial age may exceed 2 Ma.

Finally, we cannot exclude the potential influence of multi-grain averaging effects on the final ESR dose estimates (e.g., Duval et al., 2017). While we do not have evidence suggesting the presence of various populations of quartz grains with different transport and bleaching histories, it is possible that the depositional environment associated to the clayey-silty fossil horizon where 19GFS-E1 was initially collected (Parés et al., 2023) may have offered less favourable conditions to ensure the presence of one single population of fully bleached quartz grains (see Voinchet et al., 2015), in contrast to 22GAF-E1 (i.e., taken from coarser deposits resulting from a higher energy transport). However, at this stage the hypothesis can hardly be tested, since single-grain ESR measurements remain highly experimental (e.g., Beerten and Stesmans, 2006b).

5.1.3. TCN dating

Here we evaluate the model burial ages regarding post-depositional production and pre-burial complex history that would potentially lead to age underestimation and overestimation, respectively.

5.1.3.1. Post-depositional production and possible underestimation. The samples were collected at elevations 865 m.a.s.l. (22GAF-TCN1) and 823 m.a.s.l. (22GAF-TCN2) and current depths from the summit of the high plateau (933 m.a.s.l. elevation) are ~ 70 m and ~ 110 m, respectively. These depths are generally regarded more than sufficient to effectively shield the material from post-depositional cosmic ray exposure. We estimated post-depositional nuclide production considering muon interaction (based on Balco, 2017) assuming sediment density of 2 g/cm^3 and representative denudation rates for relict surfaces in the Atlas region of 15–20 m/Ma (Clementucci et al.), indicating that post-depositional productions are insignificant compared to the measured nuclide concentrations for the both samples ($< 4\%$ for ^{10}Be and $< 17\%$ for ^{26}Al , which are within uncertainties of each nuclide, i.e., 8 % and 14–21 %, respectively; **Table 4**). This exercise confirms that shielding depths are sufficient to assume no post-depositional production. Hence, in the absence of apparent analytical errors, we currently do not have a clear explanation for the significantly underestimated age obtained for the sample 22GAF-TCN2. We cannot exclude that the different outcrop geometries at the two sampling sites may have somewhat impacted post-depositional nuclide production: while the sample 22GAF-TCN1 was collected from the near-vertical cliff surface that has

most likely exposed relatively recently, the sample 22GAF-TCN2 is at the foot-slope of the tableland and thus, locally, this sample has shallower depth ($<\sim 10$ m) in current setting (Fig. 3). If this age underestimation is due to unaccounted post-depositional nuclide production, e.g., from lateral exposure from the slope surface, we might be able to solve it by applying the isochron burial dating (e.g., Balco and Rovey II, 2008; Granger, 2014; Fujioka et al., 2022). The isochron approach allows to explicitly evaluate post-burial nuclide production by measuring several clastic materials in a target horizon. While in this study we specifically aimed at cross-dating the same sandy layer using both ESR and TCN methods, in the light of the results obtained for sample 22GAF-TCN2 we will specifically explore the possibility of applying the isochron burial dating on the conglomerate layers of the sequence in the future, although its feasibility will mostly depend on the availability of quartzose clasts.

5.1.3.2. Prior burial and possible overestimation. When quartz grains had experienced complex history before depositing at a sampling site, initial $^{26}\text{Al}/^{10}\text{Be}$ ratio may be lower than the nominal ratio of 6.75 and the calculated model burial age must be regarded as the maximum estimate (Granger, 2014). Such complex history includes prolonged periods of prior burial for more than a few hundred thousand years and/or non-steady state erosion at the sediment source. Considering that the pre-Quaternary sedimentary dynamics of the High Plateaus Basin remains largely unknown, it is impossible to accurately reconstruct paleo-landscape and the paleo-drainage network in detail over a long period of time (up to a few Ma in our case). However, due to the predominance of limestone and chert clasts in the lithology of the clasts forming the conglomerates in Unit 1, we assume that these alluvial sediments were likely sourced locally from the Mesozoic-Paleozoic margin of the basin, located a few km N of the site (Parés et al., 2023). The postulated source area displays gently sloped hills without large areas of cliffs, escarpments or landslide scars and therefore barely exhibits non-steady state erosion processes (such as mass failure, plucking). Due to the apparent short distance of sediment transport as well as the absence of any evidence suggesting the presence of fluvial terraces between the sediment source and the sampled site, a prior burial for a period exceeding a few hundred thousand years is also considered highly unlikely. Should sediment transport be longer and more complex than initially assumed (as it could be tentatively deduced from the rounded clasts in the conglomerates of the lower part of the DI section), with sediment originating from other uplifted areas further south and/or east of the basin, and possibly experiencing episode(s) of prolonged pre-burial at depth during the transport, the burial age calculated above under the assumption of the simple scenario would then be regarded as a maximum possible estimate. In other words, the hypothesis of a long-distance transport of sediment and potential pre-burial episode(s) could possibly explain the age difference, or at least part of it, observed between the ESR and TCN ages of 2.75 ± 0.23 Ma and 3.35 ± 0.51 Ma, respectively. However, this scenario is currently highly speculative. Further lithological and sediment provenance studies are required to properly reconstruct the evolution of sedimentary dynamics and obtain a better understanding of the paleodrainage systems of the basin during the Plio-Pleistocene, in order to thoroughly evaluate the plausibility of such hypothesis.

In the meantime, we can reasonably hypothesize that both of our TCN samples likely did not experience complex exposure history before the current deposition, and since there is no evidence pointing to a possible age overestimation, we conservatively consider the age of 3.35 ± 0.51 (or ± 0.59 external error; Table 4) Ma as the most reasonable estimate of the burial age for sample 22GAF-TCN1.

5.2. Combining ESR and TCN dating results

A given layer located about 5 m below the fossiliferous horizon

Guefaït-4 was numerically dated by means of two independent methods applied to the same material (quartz), providing Ti ESR and TCN ages of 2.75 ± 0.23 Ma (1σ ; Table 3) and 3.35 ± 0.59 Ma (1σ external error; Table 4), respectively. Importantly, although these results differ by ~ 0.60 Ma, they may nevertheless be regarded as consistent given the significant overlap of their respective 1σ uncertainties. Consequently, while we do acknowledge the chronological difference, which may be partly related to the existing uncertainty associated to each individual method (see sections 4.1, 4.2 and 5.1.2 and 5.1.3), both ages may be currently regarded as equally reliable from a methodological point of view. There is currently no evidence suggesting that one age result should be preferred over the other: they are 1σ consistent, and are therefore being used together for the following chronostratigraphic interpretation. More specifically, these two age results show a 1σ and 2σ overlap of between 2.76 and 2.98 Ma, and 2.17 and 3.20 Ma, respectively. When considering the former, a combined ESR-TCN age of 2.87 ± 0.11 Ma (1σ) may be obtained for the layer being dated by the two methods. Alternatively, a very close weighted mean age of 2.83 ± 0.21 Ma (1σ) may also be proposed. Either way, from a chronostratigraphic point of view these dating results provide a maximum age constraint for the overlying Guefaït-4 fossil horizon.

5.3. Chronostratigraphic implications

5.3.1. Correlating DI section to the GPTS

Considered individually or in combination, the ESR and TCN results discussed above consistently support a Gauss age (3.60–2.61 Ma) for the magnetozone N1, thus favouring options 1 and 3 of Parés et al. (2023). This GPTS correlation enables to provide a reliable minimum age constraint of 2.61 Ma for the layer being numerically dated, which is compatible with the combined ESR-TCN 1σ age range of 2.76–2.98 Ma proposed above.

Consequently, the two short reverse intervals identified at about 18 and 31 m (Fig. 2) may be tentatively correlated to the short, intra-Gauss, Mammoth (3.30–3.21 Ma) and Kaena (3.12–3.03 Ma) Subchrons, as initially suggested by Parés et al. (2023). Assuming no major sedimentary hiatus, the most reasonable interpretation of the upper part of the sequence would consist of correlating normal intervals N2 and N3 the intra-Matuyama normal Subchrons that immediately follow Gauss Chron i.e., Feni (2.16–2.12 Ma) and Olduvai (1.93–1.78 Ma) Subchrons (Fig. 2). This is the Option 1 initially proposed by Parés et al. (2023). However, for completeness, we should mention that Parés et al. (2023) also considered a correlation of N2 and N3 to Olduvai Subchron and Brunhes Chrons (Option 3), an interpretation that implies protracted hiatuses in order to explain the absence of Cobb Mountain and Jaramillo Subchrons and therefore less likely. Still, there is currently no numerical age available for the upper part of the sequence that could help evaluating the reliability of each of the two options. Consequently, this evaluation has to be tentatively achieved by other means.

5.3.2. Estimated sediment accumulation and incision rates

The paleomagnetic reversals identified along the sequence may be used as chronostratigraphic tie points in order to estimate bulk, averaged sediment accumulation rates (SAR). For the lower half of the sequence (i.e., Units 1 and 2 and base of Unit 3, from 0, to 72–78 m), the main sources of uncertainty are related to (i) the exact position of the N1-R1 reversal and (ii) the relatively low sampling resolution for the lowermost deposits.

First, while there is little uncertainty on the correlation of the N1-R1 reversal to the Gauss-Matuyama transition (2.61 Ma), its exact position may be interpreted in two different ways (Fig. 2), which has non-negligible implications as far as sedimentation rates. More specifically, the low sampling resolution above Unit 2 i.e., at the base of Unit 3 between 72 and 78 m induces some uncertainty in the precise location of the reversal. In other words, the N1-R1 reversal may be tentatively positioned either at the top of Unit 2, i.e., with the last samples showing

clear normal polarity (elevation = 72 m; Scenario 1), or about 6 m above (elevation = 78 m; Scenario 2) where paleomagnetic data show a transitional VGP latitude around 0 (Fig. 7 in Parés et al., 2023), which could be effectively resulting from the Gauss-Matuyama reversal. To sum up, such uncertainty translates into a total of 6 m.

Second, the lowermost 50 m of the sedimentary sequence show a relatively low sampling resolution, with on average 1 paleomagnetic sampling station every 3 m. This has implications as far the exact position and the thickness (and the associated time range) of the short reversals identified at 18 and 31 m, for which an uncertainty of ± 3 m may be reasonably considered.

Consequently, when considering all the various sources of uncertainty involved as well as the relative short duration of the Mammoth and Kaena Subchrons, and assuming a relatively steady (although quite unlikely) sedimentation across units 1 and 2, calculated sediment accumulation rates vary from 7.1 to 11.6 cm/ka, while an overall SAR of about 9.2 ± 1.3 cm/ka (1 standard deviation) may be estimated. With this value, the age of the base of the section may be estimated to ~ 3.4 Ma (scenario 1: ~ 3.39 Ma; Scenario 2: ~ 3.45 Ma). Importantly, this is compatible with the paleomagnetic evidence constraining the deposits to <3.60 Ma given their normal polarity correlated to Gauss chron (3.60–2.61 Ma). Moreover, a SAR-inferred age of 2.75 Ma (scenario 1: ~ 2.72 Ma; Scenario 2: ~ 2.78 Ma) may be estimated for the deposits corresponding to the ESR/TCN sample 22GAF-E1/TCN1. While this result is in closer agreement with the ESR age of 2.75 ± 0.23 Ma, it is not incompatible with the TCN result either given the large associated error (3.35 ± 0.51 Ma). It is actually consistent with the combined ESR-TCN age of 2.87 ± 0.11 Ma, providing thus a semi-independent validation of the numerical ages.

Extrapolating this SAR value of ~ 9 cm/ka to the upper part of the sequence would result in apparent ages for the reversals that are systematically older by > 100 ka than the known ages of the subchrons, i.e. making it incompatible with Option 1 or 3 of Parés et al. (2023). In other words, this indirectly suggests that the SAR value has decreased in the upper half of the sequence (i.e., above 72–78 m), which is consistent with lithological evidence (as observed elsewhere in a similar fluvio-lacustrine depositional environment; e.g., Pla-Pueyo et al., 2011) documenting a higher proportion of palustrine-lacustrine carbonate deposits, typical of a low-energy depositional environment, while the lower half (mostly Unit 1) is dominated by clastic sediment (Fig. 2). Actually, considering either option 1 or 3 would result in lower SAR values of ~ 5.8 cm/ka and ~ 3.1 cm/ka for the post-Gauss deposits, respectively. In this context, option 1 of Parés et al. (2023) would indicate a less abrupt change of sediment accumulation rate along the sequence compared to option 3. Consequently, the most parsimonious chronostratigraphic interpretation would be to correlate N2 and N3 to Feni and Olduvai Subchrons (Option 1) as already pointed out by Parés et al. (2023). This implies that SAR values would have varied between 5 and 10 cm/ka along the sequence (Fig. 2), with an overall decreasing trend from the bottom to the top, although we do acknowledge the need to obtain further independent age control on the upper part of the sequence in order to confirm this hypothesis. Regardless, interestingly, the magnitude and the general trend of SAR values observed for the DI section are close to those estimated from similar depositional environments further N, in the Fonelas-P1 section of the intramontane Guadix-Baza basin (Spain) located within the Betic Cordillera. There, SAR values of 5.2 cm/ka were calculated for the lowermost deposits predating the Olduvai Subchron, while a significant decrease can be observed after ~ 1.8 Ma, which coincides with a major change in the lithology with which palustrine-lacustrine carbonates replacing a siliciclastic-dominated sedimentation (Pla-Pueyo et al., 2011).

Finally, these results indirectly provide some interesting insights into incision rates for the NW part of the Za River basin. Considering the difference in the respective elevations of the top of the section and of the current river channel (~ 150 – 160 m), and assuming that the top of the section, of Olduvai age (~ 1.8 Ma), marks the end of the sedimentation in

the area and the beginning of the valley incision, an incision rate of 0.08 mm/a ($=8$ cm/ka) may be roughly estimated. We do acknowledge the limitations of this crude calculation, given the significant uncertainty around the evolution of the sedimentary dynamics in the basin following the deposition of Unit 4 sediments, and because based on the (unlikely) assumption of a steady incision rate over time. Additionally, this value should be regarded as a minimum estimate, since (i) an additional sedimentation posterior to unit 4, or (ii) a delayed incision, would both induce the calculation of higher incision rates. For example, a valley incision starting around the Brunhes-Matuyama transition (0.77 Ma; i.e., Option 3 of Parés et al., 2023) would result in a rate estimate of ~ 0.2 mm/a. Consequently, regardless of whether GPTS correlation options 1 or 3 is preferred for the uppermost N3 interval, calculations return minimum incision rates of ~ 0.1 – 0.2 mm/a, which are compatible, and within relatively close range to the estimate of ~ 0.3 mm/a obtained earlier by Pastor et al. (2015) for the Middle to Late Pleistocene time range in the nearby Missour Basin, which also belongs to the Moulouya River Catchment (Fig. 1).

This preliminary estimate needs, however, further confirmation by a solid set of dating results for the most recent deposits marking the end of the main phase of endorreic sedimentation in the NW part of the Za River Catchment, as well as for the fluvial terraces related to the Pleistocene fluvial incision in order to obtain robust chronological tie-points to rely on for a more reliable evaluation of the bulk, recent incision rates.

5.3.3. The age of Guefai-4 fossil horizon

On the one hand, the combination of the existing magnetostratigraphic and chronometric evidence enables to correlate the fossil horizon of Guefai-4 to the Gauss Chron, providing thus a minimum age constraint of 2.61 Ma. On the other hand, numerical dating results from a layer positioned stratigraphically below the fossil horizon returns a maximum age constraint of 2.76–2.98 Ma (2.87 ± 0.11 Ma).

When using the mean SAR value of 9.2 ± 1.3 cm/ka estimated from the paleomagnetic data for the lower part of the sequence, interpolated age estimates of ~ 2.73 Ma (scenario 2) and ~ 2.66 Ma (scenario 1) may be obtained for the fossil horizon GFT-4, although this needs to be taken with caution given the presumed changes in sediment accumulation as anticipated from the sedimentary facies. Importantly, this result is compatible with the independent age control given by the numerical dating methods. Instead, when considering the upper and lower range of the combined ESR-TCN age (2.76 and 2.98 Ma), and the uncertainty on the position of the N1-R1 transition (72 or 78 m), a lower mean SAR value of 6.1 ± 3.5 cm/ka may be estimated for the deposits in between, mostly covering Unit 2, which seems compatible with the observed lithology (i.e., dominantly carbonated). Interestingly, it may be noted that this SAR value for Unit 2 is close to that estimated earlier from Option 1 for the upper part of the sequence with similar lithology (~ 5.8 cm/ka), providing thus indirect additional support to this hypothesis. Based on this result, an age of ~ 2.79 Ma (scenario 2) and ~ 2.69 Ma (scenario 1) may be interpolated for the fossil horizon.

In conclusion, regardless of the scenario and approach employed, the SAR-inferred age for Guefai-4 vary within relatively small range between ~ 2.69 and ~ 2.79 Ma, and may be estimated to 2.72 ± 0.05 Ma (1 standard deviation) on average. Consequently, an age of ~ 2.7 Ma may be reasonably proposed for Guefai-4. The compatibility of this new dating result with biochronological inferences, and in particular those based on the recent taxonomic revision of the large mammal assemblage carried out by one of us will be further evaluated hereafter.

5.4. Biostratigraphic and biochronological implications

5.4.1. Rodent fossil record

Rodent species are usually regarded as excellent tools for biostratigraphic correlations and biochronological inferences. By positioning the rodent assemblage from Guefai-4 on a more secure timeline, the present study can help enhance our understanding of the chronological ranges of

northern African rodent species, and especially when considering that none of the Pliocene localities reported by Stoetzel (2013) have independent numerical age control. Among the various taxa reported by Piñero et al. (2020) (see also Table 1), the murids *Golunda aouraghei*, *Praomys cf. skouri*, *Paraethomys pusillus*, and *Paraethomys chikeri* are the most significant for biostratigraphic purposes.

Guefaït-4 is the type locality of *Golunda aouraghei*, a descendant of *Golunda jaegeri* (Piñero et al., 2020). *G. aouraghei* has only been identified at Guefaït-4, marking the last occurrence of the genus *Golunda* in Africa (Piñero et al., 2020). Interestingly, the new numerical age of ~2.7 Ma for Guefaït-4 implies that this genus can be used as a reliable biochronological indicator of the Pliocene in northern regions of the continent. As a consequence, the presence of *G. jaegeri* at Amama 3 (Algeria; Jaeger, 1975), Oued Athmenia 1 (Algeria; Coiffait and Coiffait, 1981; Coiffait-Martin, 1991), Oued Smendou (Coiffait-Martin, 1991), and Azib (Aït Kandoula, Morocco; Benammi et al., 1996; Zouhri et al., 2017; Zouhri and Amane, 2022) therefore supports an older Pliocene age for these fossil localities.

In contrast, the presence of *Praomys cf. skouri* in Guefaït-4 implies that it may not serve as a marker of the beginning of the Early Pleistocene in the continental record of northern Africa, as previously proposed (Stoetzel, 2013). Instead, our results indicate that the first appearance of this taxon occurred during the Late Pliocene, although near the Plio-Pleistocene boundary. Furthermore, the ~2.7 Ma age for Guefaït-4 is consistent with the previous Pliocene age inference for various localities where *Paraethomys pusillus* has also been recorded, such as Oued Smendou (Coiffait-Martin, 1991), Oued Mellegue (O.M.) Voie Ferrée (Tunisia; Robinson et al., 1982; Coiffait-Martin, 1991), and Azib (Aït Kandoula, Morocco; Benammi et al., 1996; Zouhri et al., 2017). So far, this murid species has been exclusively found in deposits assigned to the Pliocene (Stoetzel, 2013).

Finally, *Paraethomys chikeri* is very abundant in Guefaït-4 (25 % of the whole rodent assemblage; see Supplementary Information in Ramírez-Pedraza et al., 2024), it is also common in the N African localities that are traditionally biochronologically constrained to the Early Pleistocene (Stoetzel, 2013), such as Ahl al Oughlam (Morocco; Geraads, 1995; Geraads et al., 2010), Argoub Kemellal 2 (Algeria; Coiffait-Martin, 1991), Bulla Regia 1 (Tunisia; Jaeger, 1975; Mein and Pickford, 1992), Irhoud Ocre (Morocco; Jaeger, 1975), and Djebel Ressas 1 (Tunisia; Mein and Pickford, 1992). The earliest report of this species, however, comes from O.M. Voie Ferrée (Tunisia; Robinson et al., 1982; Coiffait-Martin, 1991), a site with debated chronology (see Stoetzel (2013) and references therein), which has been previously regarded as biostratigraphically slightly older than Guefaït-4, as suggested by the presence of *Praomys cf. skouri* at the latter (Parés et al., 2023). Consequently, the ~2.7 Ma age for Guefaït-4 does provide an additional minimum age constraint for O. M. Voie Ferrée, which most likely dates back to the Late Pliocene, and for the first appearance of *P. chikeri*.

Our results have also implications regarding the general biozonation initially proposed by Stoetzel (2013) for the Neogene-Quaternary rodent fossil record of N Africa. For example, the composition of Biozone 6 covering the entire Pliocene of northwestern Africa should also include *P. chikeri* and *P. skouri*, whereas these taxa were previously considered as exclusive to Biozone 7 (Early Pleistocene). Alternatively, a subdivision of the Pliocene biozone may be considered, with the creation of a new Late Pliocene sub-biozone. Additionally, it is confirmed that the rodent *Paraethomys chibensis* (phylogenetic ancestor of *P. chikeri*) is exclusively Pliocene (Coiffait-Martin, 1991). Simultaneously, it is also corroborated that *Paraethomys rbiae* (phylogenetic descendant of *P. chikeri*) is restricted to the Pleistocene, as suggested in previous studies (e.g., Jaeger, 1975; Mein and Pickford, 1992; Martínez-Navarro et al., 2014).

Finally, our results do also provide an indirect age constraint to the Moroccan locality of Ahl al Oughlam, which has delivered one of the richest and most diverse Plio-Pleistocene fossil assemblage in N Africa (e.g., Geraads, 2006; Geraads et al., 2010), although no geochronology exists so far to constrain the age of the site. The morphological features

of the molars of *P. chikeri* from Guefaït-4, such as molar size, the occasional presence of t9 on the second upper molar, and the presence of a well-developed labial cingulum on the second lower molar (Geraads, 1995), are comparable to those of *P. chikeri* from Ahl al Oughlam. However, the molars from Guefaït-4 exhibit less developed longitudinal crests compared to those from Ahl al Oughlam. This, along with the presence of *P. pusillus* and *G. aouraghei* in Guefaït-4, suggests that Ahl al Oughlam is slightly younger than Guefaït-4. Consequently, a maximum age of ~2.7 Ma may be proposed for Ahl al Oughlam, which is compatible with the initial estimation of ~2.5 Ma based on biochronology (Geraads et al., 2010).

5.4.2. Large mammal fossil record

While the ~2.7 Ma age for Guefaït-4 proposed here provides an independent validation of the initial biochronological assessment made by Parés et al. (2023), the recent taxonomic revision of the large vertebrate fauna from Guefaït-4 by one of us (J. van der Made) has enabled to update the composition of the fossil assemblage (see Table 1). This may offer new perspectives regarding biochronological inferences and implications, which may be summarized as follows (note that a detailed taxonomic evaluation and discussion will be found in a forthcoming paper by Van der Made et al., in prep.).

The various taxa identified (see Table 1) in the faunal assemblage are not equally relevant from a biochronological point of view. Some of them have been identified with only few remains, sometimes fragmented, precluding a precise taxonomic attribution to the genus or species level (see Table 1). Others show a relatively long temporal distribution (e.g., *Macaca*, *Dinofelis*), and thus do not provide any tight age constraint. Other taxa (e.g., *Centrochelys*, *Felis*, *Eucyon*) have been found at sites that are regarded as biostratigraphically close to Guefaït-4 (e.g., Ahl al Oughlam), and their presence is therefore compatible with an age of ~2.7 Ma. However, there are several taxa suggesting that the fossil assemblage from Guefaït-4 may have an age significantly older than ~2.7 Ma, possibly >3.0–3.2 Ma, such as *Archaeopotamus hippomensis*, *Stephanorhinus africanus*, Suidae indet. cf. *Kolpochoerus afarensis*, cf. *Ictitherium ebu* and *Hipparrison*. The compatibility of the two chronological interpretations will be evaluated hereafter, while it should be kept in mind that it is beyond the scope of the present paper to discuss in details taxonomic attributions and biostratigraphic correlations (the reader may refer to Van der Made et al., in prep., for that matter).

The hippopotamus from Guefaït-4 is a large species with gracile metapodials and large premolars. These features point to the primitive *Hexaprotodon* and *Archaeopotamus*. The known features are compatible with *Archaeopotamus harvardi* and the North African “*Hexaprotodon*” *hippomensis*, which probably is an *Archaeopotamus*, while *Hex. sahabiensis* and *Hex. andrewsi* are smaller. *Archaeopotamus* is supposed to have dispersed into North Africa, southern Europe and the Arabian Peninsula during the latest Miocene (Martino et al., 2023). By the time of Ain Boucherit Lower level (2.44 ± 0.14 Ma), those primitive hippos were replaced by *Hippopotamus* (Sahnouni et al., 2018), providing thus a minimum age constraint for the last occurrence of *Archaeopotamus*. In this context, although the specimen from Guefaït-4 is very primitive and shows similarities with specimens from Late Miocene-Early Pliocene localities, an age of ~2.7 Ma is not incompatible with our (limited) current knowledge about N African hippo.

Stephanorhinus africanus, identified at Guefaït-4, was first recognized at Ichkeul (Tunisia) (Arambourg, 1970), for which a biochronologically-inferred Pliocene age of about 4.6–3.8 Ma (Werdelin, 2010; Stoetzel, 2013 and references therein) or 3.2–3.0 Ma (Van der Made et al., 2022) has been proposed. Further, the presence of *Stephanorhinus* has also been reported at Koro Toro 13 (Chad), which has been constrained to 3.0–3.5 Ma based on biochronology (Brunet et al., 1997). The species is rare and for this reason its temporal distribution is not well known. In addition, there is no independent age control for the sites from which it is known. *Stephanorhinus africanus* has very low crowned molars, which are lower than in *S. etruscus* and more similar to

the teeth of the Pliocene species of western Eurasia. Two of them are known from MN15 (about 5–3.5 Ma for Guérin, 1980; or 4.2–3.5 Ma based on Ezquerro et al., 2022), while *S. jeanvireti* is known from MN16 (3.5–2.6 Ma or 3.5–>2.0 Ma) (Guérin, 1980). Possibly the last site with the latter species is Montopoli (Guérin, 1980), where the fossiliferous level is situated a few metres above a magnetostratigraphic reversal tentatively interpreted as the Gauss-Matuyama boundary (Lindsay et al., 1980). This minimum age constraint of 2.61 Ma should however mostly be regarded as indicative given the methodological limitations highlighted by the authors themselves, and the absence of minimum details regarding the method employed and results obtained. It is possible that *S. africanus* descended from a species that dispersed into North Africa and survived longer than the Eurasian species. Consequently, we do acknowledge that the existing record of *Stephanorhinus* in N Africa and the primitive aspect of the Guefai-4 specimens both might suggest an age older than ~2.7 Ma, but that they do not rule out such an age.

Very poor remains of a suid ($n = 5$) attributed to Suidae indet. cf. *Kolpochoerus afarensis* include fragments of low crowned molars and a large second upper deciduous molar (D^2). The morphology of the latter excludes the Tetraconodontinae. The low crowned molars exclude most of the African Suinae, such as *Metridiochoerus* and the later species of *Kolpochoerus*. The dimensions of the remains are compatible with *K. afarensis*, which has so far not been reported with certainty from N Africa. This species gave rise to *K. limnetes* (Cooke, 1985). White (1996) indicated the last appearance of the former to be ~2.5 Ma and the first appearance of the latter at 2.9 Ma, while Cooke (2007) indicated both to occur in member C of the Shungura Fm (2.92–2.53 Ma) in E Africa. While there is no further information in the literature on whether there was a gradual evolution or whether both species co-existed for some time (i.e., one might question whether ancestor and descendant coexisted during 0.4 Ma in a small area), the ~2.7 Ma age for cf. *K. afarensis* at Guefai-4 is presently compatible with the published information in E Africa. Finally, the species from Guefai-4 could also be, or be a descendant of, a Eurasian species. Some of these have been suggested to have dispersed to Africa. The European *Sus arvernensis* is smaller, while *Propotamochoerus provincialis* could fit, but last occurred in MN15 (4.2–3.5 Ma; Ezquerro et al., 2022), and which could possibly imply an age older than ~2.7 Ma for the specimen from Guefai-4. The presence of *P. provincialis* in Africa remains, however, hypothetical (Van der Made et al., in prep.), giving thus less weight to this option for the moment, until this question is further investigated in the future.

The presence of Hyenaenidae at Guefai is evidenced by a couple of identified remains only, including a very small and narrow P_4 attributed to cf. *Ictitherium ebu* (see Van der Made et al., in prep.), which is last known from the Apak Member of the Lothagham Fm (E Africa), dated to between 5 and 4.2 Ma (Werdelin, 2003, 2010), or to a still older species. Consequently, the biochronology may point towards a much older age than ~2.7 Ma age for the specimen from Guefai-4, making it incompatible with the numerical age results in the first instance. However, the limited number of remains identified at Guefai-4 ($n = 2$), as well as the absence of comparative specimens in the North African fossil record, indicate that very little is known about Pliocene Hyenaenidae in N Africa. We cannot exclude that, if the hyaena from Guefai 4 belongs to one of the known African species, it may have survived longer in North Africa than south of the Sahara. Comparisons with Eurasian species will be discussed in Van der Made et al. (in prep.).

Finally, the hipparion from Guefai-4 is similar to *Hipparium sitifense*, without ectostylids, which, according to Arambourg (1956, 1970), was replaced by *Stylohipparion libycum*, with such stylids in the lower cheek teeth. The latter is at present placed in the genus or subgenus *Eurygnathohippus*, which evolved south of the Sahara and dispersed north. North African *Eurygnathohippus* fossils were collected at Oued Akrech and Fouarat from sands that also yielded *Pecten benedictus* (van der Made et al., 2022 and references therein). That bivalve may be tentatively used to infer a chronological constraint for the replacement of one type of hipparion by another. It has a last appearance in faunal unit MPMU 1

of Monegatti and Raffi (2001), the upper boundary of which has been initially constrained by the authors to around 2.9–3.0 Ma. This would imply that the dispersal of *Eurygnathohippus* to North Africa occurred after that date and, if Arambourg's hypothesis is correct, that hipparions without ectostylids went extinct before ~2.9 Ma (Van der Made et al., 2022). However, Oued Akrech and Fouarat lack independent chronological control and the minimum age constraint 2.9–3.0 Ma is based on multiple correlations, which leads to a very large temporal uncertainty. Moreover, the hipparion from Guefai-4 is not identical to *H. sitifense* (see further details in Parés et al., 2023), and we cannot exclude that the small differences might be due to either intra-species variability, or a different grade of evolution. The latter would imply a different age for Guefai-4, either older or younger, from the localities with *H. sitifense*. Finally, it is also possible that the dispersal of *Eurygnathohippus* does not coincide with the last appearance of hipparions without ectostylid (including *Hipparium sitifense* and the hipparion from Guefai 4). The two forms of hipparion may have co-existed during some time. While the biochronological ages of the known localities with *Hipparium sitifense* are based on the assumption that *H. sitifense* preceded *Eurygnathohippus* in North Africa, none of them has actually been independently dated. Although we acknowledge that the sites with *H. sitifense* did not yield fossils of other species that suggest a younger age than 2.9 Ma, on the one hand they have very short faunal lists, and, on the other hand the existing uncertainty around their chronology and on our understanding of the evolution of *Hipparium*, are presently not incompatible with the new dating results obtained in this work.

To sum up, although some of the large mammals might suggest an age older than ~2.7 Ma, chronostratigraphic and biochronological evidence would nevertheless be compatible under the conditions that the record of these species in Guefai-4 : (i) is chronologically close to their last known or inferred record in Africa (Suidae indet. cf. *Kolpochoerus afarensis*) or in North Africa (*A. hippoensis*); (ii) is chronologically close to the last record of species with a similar grade of evolution (*Stephanorhinus africanus*); (iii) persisted much later in North Africa later than in other parts of Africa or even the world, due to isolation or a different environment there (*Ictitherium*); (iv) is younger than the dispersal of *Eurygnathohippus* to North Africa (*Hipparium aff. sitifense*).

6. Conclusion

Dating archaeo-paleontological localities beyond 1 Ma in non-volcanic context remains highly challenging (see also Duval et al., 2023). So far, combining numerical dating methods with magnetostratigraphy and biostratigraphy/biochronology has proven to be the most efficient way to provide secure chronological constraints to Plio-Pleistocene deposits in North Africa (e.g., Sahnouni et al., 2018; Bartz et al., 2018, 2019a,b; Duval et al., 2018, 2021). Such a combined approach enables to compensate for the intrinsic limitations and uncertainties associated to each individual line of evidence available, which is very well illustrated by the present study.

From a methodological point of view, this work contributes to a better understanding of the potential and current limitations of ESR and TCN methods to date fluvio-lacustrine deposits beyond 2.6 Ma. Over such a long time range, a special attention should be paid to a number of sources of uncertainty, as they may have a non-negligible impact on the final age result. In ESR dating, this is the case for example with the DRC fitting uncertainty, the heterogeneity of the sedimentary environment, and the estimation of the long-term water content. In TCN burial dating, some knowledge about the pre-burial transport and deposition conditions, as well as about the post-depositional processes (e.g., erosion) that may potentially lead to (near-)surface exposure, is critical for the use of a simple burial model. Adjusting sampling strategy by targeting the most suitable deposits also appears to be crucial in order to obtain methodologically reliable results. In this context, ESR sampling should preferably focus on quartz-rich fine sand deposits with a low amount of clays and showing a relatively low radioactivity (<1000 $\mu\text{Gy/a}$) in order to

maximize the probability of optimal bleaching conditions and minimize the possibility of inaccurate dose estimation. In comparison, multiple sampling of cobble-to-boulder size quartz-rich clasts from a given layer for isochron TCN burial dating would enable to explicitly evaluate post-burial nuclide production.

Despite these complications, which resulted in some age scatter and underestimation, these two independent numerical dating methods nevertheless provide useful and consistent new chronological constraints for the lower part of the Dhar Iroumyane section. In particular, a combined ESR-TCN age of 2.87 ± 0.11 Ma may be proposed for a layer positioned in the upper part of Unit 1, providing a maximum age constraint for the stratigraphically overlying Guefaït-4 fossil horizon. Importantly, this age is compatible within uncertainties with the other lines of evidence provided by the magnetostratigraphy and the biochronology. Based on SAR estimates derived from the magnetostratigraphy and numerical dating results, a Late Pliocene age of ~ 2.7 Ma may be proposed for Guefaït-4. When considered together, the various lines of evidence available enable to establish a coherent chronostratigraphic framework by correlating the N1-R1 transition to the Gauss-Matuyama magnetic reversal (2.61 Ma), while the short reverse intervals identified in the lower part of the section may reasonably be correlated to Mammoth (3.33–3.21 Ma) and Kaena (3.12–3.03 Ma) Subchrons. In contrast, the upper part of the sequence is less securely correlated to the GPTS given the absence of independent age control available, although we discuss observations supporting the probable correlation of N2 and N3 intervals to Feni (2.16–2.12 Ma) and Olduvai (1.93–1.78 Ma) Subchrons (Fig. 2). However, given the limited number of samples in the present study, additional numerical age results are required along the sequence in order to further support this chronological interpretation and reinforce the promising chronostratigraphic framework established for the Dhar Iroumyane section. In particular, future investigations will especially focus on (i) increasing sampling resolution for ESR and TCN methods in the uppermost deposits to definitely confirm this correlation, and (ii) exploring the possibility of applying the TCN isochron burial dating to conglomerate levels of the lower part of the section, if large-size quartzose clasts are available, to evaluate post-depositional production and strengthen the burial dating results obtained in this study.

Interestingly, our results also provide some insights into sedimentation dynamics, which may complement and support lithological observations. More specifically, a non-negligible variability of sediment accumulation rates may be evidenced along the sequence, with overall decreasing values from the bottom to the top of the sequence, which is on the other hand expected from lithological evidence and the evolution of depositional environment (and consistent with other studies based on similar deposits; e.g. Pla-Pueyo et al., 2011), with dominantly clastic sediments present in the lower half and continental carbonates in the upper half of the section.

Finally, by contributing to strengthen the age constraints on Guefaït-4, the present study aligns with recent significant efforts in increasing the chronological resolution and accuracy of the N African fossil record (e.g., Gallotti et al., 2021; Sahnouni et al., 2018; Duval et al., 2021, 2023) by means of magnetostratigraphy and numerical dating methods. This remains, however, an ongoing work, as many fossil assemblages still lack a robust independent age control (e.g., Ahl al Oughlam, Ichkeul, Fouarat, O.M Voie Ferrée, Ain Jourdel, Oued Akrech, Ain Brimba; see Stoetzel, 2013; Van der Made et al., 2021 and references therein), which naturally adds intrinsic uncertainty to biochronological inferences and may explain, at least partially, the apparent potential discrepancy between the age of ~ 2.7 Ma proposed here for Guefaït-4 and the presence of a few taxa possibly pointing to a somewhat older age. Regardless, about one decade of multi-disciplinary investigations has enabled to build a comprehensive picture of the site and of its chronostratigraphic, paleoenvironmental and paleoecological context (e.g., Alba et al., 2021; Piñero et al., 2020; Madurell-Malapeira et al., 2021; Van der Made et al., in prep.; Parés et al., 2023; Ramírez-Pedraza

et al., 2024), converting Guefaït-4 into a key fossil locality, and one of the richest and most diverse faunal assemblages of the Plio-Pleistocene N African fossil record beyond 2 Ma.

Declaration of competing interest

The authors declare that they have no known competing financial interests or personal relationships that could have appeared to influence the work reported in this paper.

Acknowledgements

We thank Jerada Government and Local Authorities of Aïn Beni Mathar and Guefaït for local permits to develop geological, archaeological, and paleontological fieldworks in the region. Funding for this research was provided by: Palarq Foundation, Spanish Ministry of Culture and Sport, Spain (Ref: 42-T002018N0000042853 & 170-T002019N0000038589), Faculty of Sciences (Mohamed First University of Oujda, Morocco), Direction of Cultural Heritage (Ministry of Youth, Culture and Communication, Morocco) and INSAP (Institut National des Sciences de l'Archéologie et du Patrimoine, Morocco). The Ramón y Cajal fellowships granted to M.D. (RYC2018-025221-I), A.R.-H. (RYC2022-037802-I), and P.P. (RYC2023-044218-I) are funded by MCIN/AEI/10.13039/501100011033 and by “ESF Investing in your future”. This work is also part of Grants PID2021-123092NB-C21 and PID2021-123092NB-C22 funded by MCIN/AEI/ 10.13039/ 501100011033/‘ERDF A way of making Europe’. Parts of this research were carried out at the Ion Beam Centre (IBC) at the Helmholtz-Zentrum Dresden-Rossendorf e. V., a member of the Helmholtz Association. AMS measurements at DREAMS have been supported by the RADIATE project under the Grant Agreement 824096 from the EU Research and Innovation programme HORIZON 2020 (Radiate Transnational Access Proposal# 23003288-ST). We would like to thank the DREAMS operator team for their assistance with AMS-measurements. Research Groups Support of the Catalonia Government (2021 SGR 01238 - 2023PFR-URV-01238 (URV) Palhum (AGAUR) and 2021 SGR 01237 GAPS (AGAUR)- 2023PFR-URV-01237 (URV)). The IPHES-CERCA has received financial support through the “María de Maeztu” program for Units of Excellence (CEX2024-01485-M/funded by MICIU/AEI/ 10.13039/501100011033). R.S-R, M.G.Ch., and J.A. research is funded by CERCA Programme/Generalitat de Catalunya. J.v.d.M. received funding from PID2022-137070NB-I00 and PID2021-122355NB-C33 financed by MCIN/AEI/10.13039/501100011033/FEDER, UE. M.F. is beneficiary of a Joan Oró predoctoral fellowship (2023 FI-1 00578) funded by AGAUR and the European Social Fund (ESF). We thank Dr Santiago Padilla, Ms Leticia Miguens and Mr Jorge Revilla, CENIEH for target preparation for cosmogenic nuclide dating, as well as Ms María Jesús Alonso Escarza, CENIEH, for invaluable support with the ESR dating analytical procedure. Special thanks to Prof. Gilles Rixhon, University of Strasbourg, France, for kindly providing Fig. 1A, and to Prof. Anton Wallner from HZDR for logistical arrangement for AMS measurements. Finally, we would like to thank all the people who took part in the excavation of the site from 2017 to 2019 and the restoration of the fossils to date.

Appendix A. Supplementary data

Supplementary data to this article can be found online at <https://doi.org/10.1016/j.quascirev.2025.109610>.

Data availability

All data and/or code is contained within the submission.

References

- Akhmadaliev, S., Heller, R., Hanf, D., Rugel, G., Merchel, S., 2013. The new 6 MV AMS-facility DREAMS at Dresden. *Nucl. Instrum. Methods Phys. Res., Sect. B* 294, 5–10.
- Alba, D.M., Rodríguez-Hidalgo, A., Aouraghe, H., van der Made, J., Ouja, A., Haddoumi, H., Saladié, P., Aissa, A., Marín, J., Farkouch, M., Lorenzo, C., Bengamra, S., Delson, E., Chacón, M.G., Sala-Ramos, R., 2021. New macaque fossil remains from Morocco. *J. Hum. Evol.* 153, 102951.
- Arambourg, C., 1956. Sur des restes d'Hippiares sitifense Pomel, des calcaires lacustres de Mascara (Oran). *Bull. Soc. Geol. Fr.* 6 (7–9), 817–827.
- Arambourg, C., 1970. Les vertébrés du Pléistocène de l'Afrique du nord. In: *Archives du Muséum national d'histoire naturelle*, 7th series, pp. 1–126, 10.
- Balco, G., 2017. Production rate calculations for cosmic-ray-muon-produced ^{10}Be and ^{26}Al benchmarked against geological calibration data. *Quat. Geochronol.* 39, 150–173. <https://doi.org/10.1016/j.quageo.2017.02.001>.
- Balco, G., Rovey II, C.W., Stone, J.O., 2005. The first glacial maximum in North America. *Science* 307, 222.
- Balco, G., Rovey II, C.W., 2008. An isochron method for cosmogenic-nuclide dating of buried soils and sediments. *Am. J. Sci.* 308, 1083–1114.
- Balco, G., Stone, J.O., Lifton, N.A., Dunai, T.J., 2008. A complete and easily accessible means of calculating surface exposure ages or erosion rates from ^{10}Be and ^{26}Al measurements. *Quat. Geochronol.* 3, 174–195. <https://doi.org/10.1016/j.quageo.2007.12.001>.
- Bartz, M., Rixhon, G., Duval, M., King, G.E., Álvarez-Posada, C., Parés, J.M., Brückner, H., 2018. Successful combination of electron spin resonance, luminescence and palaeomagnetic dating methods allows reconstructing the Quaternary evolution of the lower Moulouya River (NE Morocco). *Quat. Sci. Rev.* 185, 153–171.
- Bartz, M., Arnold, L.J., Demuro, M., Duval, M., King, G.E., Álvarez Posada, C., Parés, J.M., Rixhon, G., Brückner, H., 2019a. Single-grain TT-OSL dating results confirm an Early Pleistocene age for the lower Moulouya River deposits (NE Morocco). *Quat. Geochronol.* 49, 138–145.
- Bartz, M., Arnold, L.J., Spooner, N., Demuro, M., Campaña Lozano, I., Rixhon, G., Brückner, H., Duval, M., 2019b. First experimental evaluation of the alpha efficiency in coarse-grained quartz for ESR dating purpose: implications for dose rate evaluation. *Sci. Rep.* 9, 1–10. <https://doi.org/10.1038/s41598-019-54688-9>, 19769.
- Bartz, M., Duval, M., Brill, D., Zander, A., King, G.E., Rhein, A., Walk, J., Stauch, G., Lehmkühl, F., Brückner, H., 2020. Testing the potential of K-feldspar postIR-IRSL and quartz ESR for dating coastal alluvial fan complexes in arid environments. *Quat. Int.* 556, 124–143.
- Beerten, K., Stemsans, A., 2006a. The use of Ti centers for estimating burial doses of single quartz grains: a case study from an aeolian deposit -2 Ma old. *Radiat. Meas.* 41, 418–424.
- Beerten, K., Stemsans, A., 2006b. Some properties of Ti-related paramagnetic centres relevant for electron spin resonance dating of single sedimentary quartz grains. *Appl. Radiat. Isot.* 64 (5), 594–602.
- Benammi, M., Calvo, M., Prévot, M., Jaeger, J.-J., 1996. Magnetostratigraphy and paleontology of Aït Kandoula basin (High Atlas, Morocco) and the African-European late Miocene terrestrial fauna exchanges. *Earth Planet Sci. Lett.* 145, 15–29.
- Benzid, Timar-Gabor, 2020. Phenomenological model of aluminium-hole ($\text{AlO}_4/\text{h}^{+0}$) defect formation in sedimentary quartz upon room temperature irradiation: electron spin resonance (ESR) study. *Radiat. Meas.* 130, 106187.
- Borchers, B., Marrero, S., Balco, G., Caffee, M., Goehring, B., Lifton, N., Nishiizumi, K., Phillips, F., Schaefer, J., Stone, J., 2016. Geological calibration of spallation production rates in the CRONUS-Earth project. *Quat. Geochronol.* 31, 188–198.
- Brennan, B.J., Lyons, R.G., Phillips, S.W., 1991. Attenuation of alpha particle track dose for spherical grains. *Nucl. Tracks Radiat. Meas.* 18, 249–253.
- Brennan, B.J., 2003. Beta doses to spherical grains. *Radiat. Meas.* 37, 299–303.
- Brunet, M., Beauvilain, A., Geraads, D., Guy, F., Kasser, M., Mackaye, H.T., MacLatchy, L., Mouchelin, G., Sudre, J., Vignaud, P., 1997. Tchad: un nouveau site à Hominides Pliocène. *Comptes rendus de l'Académie des Sciences* 324, 341–345.
- Chmeleff, J., von Blanckenburg, F., Kossett, K., Jakob, D., 2010. Determination of the ^{10}Be half-life by multicollector ICP-MS and liquid scintillation counting. *Nucl. Instrum. Methods Phys. Res. Sect. B Beam Interact. Mater. Atoms* 268, 192–199.
- Clementucci, R., Ballato, P., Siame, L.L., Faccenna, C., Racano, S., Torretti, G., Lanari, R., Leanni, L., Guillou, V. Transient response to changes in uplift rates in the northern Atlas-Meseta system (Morocco). *Geomorphology* 436, 108765. <https://doi.org/10.1016/j.geomorph.2023.108765>.
- Coiffait, B., Coiffait, P.E., 1981. Découverte d'un gisement de micromammifères d'âge Pliocène dans le Bassin de Constantine (Algérie): présence d'un Muridé nouveau, *Paraethomys athemiae* n. sp. *Palaeovertebrata* 11, 1–15.
- Coiffait-Martin, B., 1991. Contribution des rongeurs du Néogène d'Algérie à la biochronologie mammalienne d'Afrique Nord-Occidentale, Ph.D. Thesis. University of Nancy, France, 1–389 (unpubl.).
- Cooke, H.B.S., 1985. Plio-Pleistocene Suidae in relation to African hominid deposits. In: Beden, M.M., Behrensmeier, A.K., Boaz, N.T., Bonnefille, R., Brain, C.K., Cooke, B., Coppens, Y., Deschamps, R., Eisenmann, V., Gentry, A., Geraads, D., Géze, R., Guérin, C., Harris, J., Koeniguer, J.C., Letouzey, R., Petter, G., Vincents, A., Vrba, E. (Eds.), *L'Environnement des hominidés au Plio-Pleistocène*. Masson, Paris, New York, Barcelona, Milan, Mexico, São Paulo, pp. 101–115.
- Cooke, H.B.S., 2007. Stratigraphic variation in Suidae from the Shungura Formation and some coeval deposits. In: Bobe, R., Alemseged, Z., Behrensmeier, A.K. (Eds.), *Hominin Environments in the East African Pliocene: an Assessment of the Faunal Evidence*. Springer -, Dordrecht, pp. 107–127.
- Demuro, M., Duval, M., Arnold, L.J., Spooner, N.A., Creighton, D.F., Méndez-Quintas, E., Santonja, M., Pérez-González, A., 2020. Insights into the relationship between luminescence and ESR dating signals from Spanish sedimentary quartz samples of different geologic origins. *Quat. Int.* 556, 165–179.
- Demuro, M., Arnold, L.J., Duval, M., Churruca Clemente, A., Santonja, M., Pérez-González, A., 2024. Extended-range luminescence and ESR dating of Iberian fluvial terraces (Duero and Guadiana basins) associated with the lower Palaeolithic sites of La Maya I, II, III, Burganes and Albalá (west-central Spain). *Quat. Geochronol.* 83, 101567. <https://doi.org/10.1016/j.quageo.2024.101567>.
- Durcan, J.A., King, G.E., Duller, G.A.T., 2015. DRAC: dose rate and age calculator for trapped charge dating. *Quat. Geochronol.* 28, 54–61 (O).
- Duval, M., 2012. Dose response curve of the ESR signal of Aluminum center in quartz grains extracted from sediment. *Ancient TL* 30 (2), 41–50.
- Duval, M., Arnold, L.J., 2013. Field gamma dose-rate assessment in natural sedimentary contexts using $\text{LaBr}_3(\text{Ce})$ and $\text{NaI}(\text{TI})$ probes: a comparison between the "threshold" and "windows" techniques. *Appl. Radiat. Isot.* 74, 36–45 (O).
- Duval, M., Guijarro, V., 2015. ESR dosimetry of optically bleached quartz grains extracted from Plio-Quaternary sediment: evaluating some key aspects of the ESR signal associated to the Ti-center. *Radiat. Meas.* 78, 28–41. <https://doi.org/10.1016/j.radmeas.2014.10.002>.
- Duval, M., Guijarro Moreno, V., Grün, R., 2013. ESR dosimetry of fossil enamel: some comments about measurements repeatability, long term signal fading and dose response curve fitting. *Radiation Protection Dosimetry* 157 (4), 463–476. <https://doi.org/10.1093/rpd/nct167>.
- Duval, M., Grün, R., Falguères, C., Bahain, J.-J., Dolo, J.-M., 2009. ESR dating of Lower Pleistocene fossil teeth: limits of the single saturating exponential (SSE) function for the equivalent dose determination. *Radiation Measurements* 44, 477–482.
- Duval, M., Arnold, L.J., Guijarro, V., Demuro, M., Santonja, M., Pérez-González, A., 2017. Electron Spin Resonance dating of optically bleached quartz grains from the Middle Palaeolithic site of Cuesta de la Bajada (Spain) using the multiple centres approach. *Quat. Geochronol.* 37, 82–96.
- Duval, M., Guijarro, V., Campaña, I., Arnold, L.J., Miguens, L., Iglesias, J., González-Sierra, S., 2018. Quantifying HF etching of quartz and feldspar coarse grains based on weight loss estimates: implication for ESR and Luminescence dating studies. *Ancient TL* 36 (1), 1–15.
- Duval, M., Sahnouni, M., Parés, J.M., van der Made, J., Abdessadok, S., Harichane, Z., Chelli, Cheheb R., Boulaghraif, K., Pérez-González, A., 2021. The Plio-Pleistocene sequence of Oued Boucherit (Algeria): a unique chronologically-constrained archaeological and paleontological record in North Africa. *Quat. Sci. Rev.* 271, 107116.
- Duval, M., Arnold, L.J., Demuro, M., Parés, J.M., Campaña, I., Carbonell, E., Bermúdez de Castro, J.M., 2022. New chronological constraints for the lowermost stratigraphic unit of Atapuerca Gran Dolina (Burgos, N Spain). *Quat. Geochronol.* 71, 101292. <https://doi.org/10.1016/j.quageo.2022.101292>.
- Duval, M., Sahnouni, M., Parés, J.M., Zhao, J.-x., Grün, R., Abdessadok, S., Pérez-González, A., Derradj, A., Harichane, Z., Mazouni, N., Boulaghraif, K., Chelli, Cheheb, R., van der Made, J., 2023. On the age of Ain Hanech Oldowan locality (Algeria): first numerical dating results. *J. Hum. Evol.* 180, 103371. <https://doi.org/10.1016/j.jhevol.2023.103371>.
- Duval, M., Arnold, L.J., Bahain, J.-J., Parés, J.M., Demuro, M., Falguères, C., Shao, Q., Voinchet, P., Arnaud, J., Berto, C., Berruti, G.L.F., Daffara, S., Sala, B., Arzarello, M., 2024a. Dating the earliest evidence of human presence in western Europe: new results from Pirro Nord (Italy). *Quat. Geochronol.*, 101519 <https://doi.org/10.1016/j.quageo.2024.101519>.
- Duval, M., Guijarro Moreno, V., Bartz, M., Alonso Escarza, M.J., Ben Arous, E., del Val, M., García Rodríguez, C., 2024b. ESR dating of quartz grains: evaluating measurement repeatability and reproducibility. *Radiat. Phys. Chem.* 215, 111313. <https://doi.org/10.1016/j.radphyschem.2023.111313>.
- Ezquerro, L., Luzón, A., Simón, J.L., Liesa, C.I., 2022. A review of the European Neogene Mammal zones from integration of litho-, bio- and magnetostratigraphy in the Teruel Basin. *Earth Sci. Rev.* 234, 104223.
- Forman, S.L., 1989. Applications and limitations of Thermoluminescence to date Quaternary sediments. *Quat. Int.* 1, 47–59.
- Fujioka, T., Chappell, J., Fifield, L.K., Rhodes, E.J., 2009. Australian desert dune fields initiated with Pliocene–Pleistocene global climatic shift. *Geology* 37 (1), 51–54.
- Fujioka, T., Fink, D., Mifsud, C., 2015. Towards improvement of aluminium assay in quartz for in situ cosmogenic ^{26}Al analysis at ANSTO. *Nucl. Instrum. Methods Phys. Res. Sect. B Beam Interact. Mater. Atoms* 361, 346–353.
- Fujioka, T., Benito-Calvo, A., Mora, R., McHenry, L., Njau, J.K., de la Torre, I., 2022. Direct cosmogenic nuclide isochron burial dating of early Acheulian stone tools at the T69 Complex (FLK West, Olduvai Bed II, Tanzania). *J. Hum. Evol.* 165, 103155. <https://doi.org/10.1016/j.jhevol.2022.103155>.
- Gallotti, R., Muttoni, G., Lefèvre, D., et al., 2021. First high resolution chronostratigraphy for the early North African Acheulean at Casablanca (Morocco). *Sci. Rep.* 11, 15340. <https://doi.org/10.1038/s41598-021-94695-3>.
- Geraads, D., 1995. Rongeurs et Insectivores (Mammalia) du Pliocène final de Ahl al Oughlam (Casablanca, Maroc). *Geobios* 28, 99–115.
- Geraads, D., 2006. The late Pliocene locality of Ahl al Oughlam, Morocco: vertebrate fauna and interpretation. *Trans. Roy. Soc. S. Afr.* 61 (2), 97–101. <https://doi.org/10.1080/00359190609519958>.
- Geraads, D., Raynal, J.-P., Sbihi-Alaoui, F.Z., 2010. Mammalian faunas from the Pliocene and Pleistocene of Casablanca (Morocco). *Hist. Biol.* 22, 275–285.
- Grün, R., 1994. A cautionary note: use of 'water content' and 'depth for cosmic ray dose rate' in AGE and DATA programs. *Ancient TL* 12 (2), 50–51.
- Guérin, C., 1980. Les rhinocéros (Mammalia, Perissodactyla) du Miocène terminal au Pléistocène supérieur en Europe occidentale. Comparaison avec les espèces actuelles. *Documents des Laboratoires de Géologie de Lyon*, 79, 3 fasc., 1–1185.

- Guérin, G., Mercier, N., Adamiec, G., 2011. Dose-rate conversion factors: update. *Ancient TL* 29 (1), 5–8.
- Guérin, G., Mercier, N., Nathan, R., Adamiec, G., Lefrais, Y., 2012. On the use of the infinite matrix assumption and associated concepts: a critical review. *Radiat. Meas.* 47 (9), 778–785.
- Guilarte, V., Duval, M., 2021. ESR dating of optically bleached quartz grains: intra-laboratory comparison of different experimental setups and their impact on dose evaluation. *Geochronometria* 48, 179–190. <https://doi.org/10.2478/geochr-2020-0005>.
- Granger, D.E., 2014. Cosmogenic nuclide burial dating in Archaeology and Paleoanthropology. In: Holland, H.D., Turekian, K.K. (Eds.), *Treatise on Geochemistry*, second ed. Elsevier, Oxford, pp. 81–97.
- Granger, D.E., Muzikar, P.F., 2001. Dating sediment burial with in situ-produced cosmogenic nuclides: theory, techniques, and limitations. *Earth Planet Sci. Lett.* 188, 269–281.
- Granger, D.E., Kirchner, J.W., Finkel, R.C., 1997. Quaternary downcutting rate of the New River, Virginia, measured from differential decay of cosmogenic ^{26}Al and ^{10}Be in cave-deposited alluvium. *Geology* 25, 107–110.
- Granger, D.E., Gibbon, R.J., Kuman, K., Clarke, R.J., Bruxelles, L., Caffee, M.W., 2015. New cosmogenic burial ages for Sterkfontein member 2 Australopithecus and member 5 Oldowan. *Nature* 522 (7554), 85–88.
- Jaeger, J.-J., 1975. Evolution des Rongeurs, du Miocène à l'actuel, en Afrique nordoccidentale. Ph.D. Thesis. University Montpellier 2, France.
- Kohl, C.P., Nishiizumi, K., 1992. Chemical isolation of quartz for measurement of in-situ-produced cosmogenic nuclides. *Geochem. Cosmochim. Acta* 56, 3583–3587.
- Korschinek, G., Bergmaier, A., Faestermann, T., Gerstmann, U.C., Knie, K., Rugel, G., Wallner, A., Dillmann, I., Dollinger, G., von Gostomski, C.L., Kossett, K., Maiti, M., Poutivtsev, M., Remmert, A., 2010. A new value for the half-life of ^{10}Be by Heavy-Ion Elastic Recoil Detection and liquid scintillation counting. *Nucl. Instrum. Methods Phys. Res. Sect. B Beam Interact. Mater. Atoms* 268, 187–191.
- Lachner, J., Rugel, G., Vivo Vilches, C., Koll, D., Stübner, K., Winkler, S., Wallner, A., 2023. Optimization of ^{10}Be measurements at the 6 MV AMS facility DREAMS. *Nucl. Instrum. Methods Phys. Res. Sect. B Beam Interact. Mater. Atoms* 535, 29–33.
- LaL, D., 1991. Cosmic ray labeling of erosion surfaces: in situ nuclide production rates and erosion models. *Earth Planet Sci. Lett.* 104, 424–439.
- Lebatard, A.-E., Bourles, D.L., Braucher, R., 2019. Absolute dating of an Early Paleolithic site in Western Africa based on the radioactive decay of in situ-produced ^{10}Be and ^{26}Al . *Nucl. Instrum. Methods Phys. Res. Sect. B Beam Interact. Mater. Atoms* 456, 169–179.
- Lin, M., Yin, G., Ding, Y., Cui, Y., Chen, K., Wu, C., Xu, L., 2006. Reliability study on ESR dating of the aluminum center in quartz. *Radiat. Meas.* 41 (7–8), 1045–1049.
- Lindsay, E.H., Lindsay, N.D., Johnson, N.M., 1980. Pliocene dispersal of the horse *Equus* and late Cenozoic mammalian dispersal events. *Nature* 287, 135–138.
- Lyons, R.G., Brennan, B.J., Hosking, P.L., 1992. Estimation of accumulated dose and its uncertainties: potential pitfalls in curve fitting. *Ancient TL* 10 (3), 42–49.
- Madurell-Malapeira, J., Rodríguez-Hidalgo, A., Aouraghe, H., Haddoumi, H., Lucenti, S. B., Ouja, A., Saladié, P., Bengamra, S., Marin, J., Souhir, M., Farkouch, M., Mhamdi, H., Aissa, A., Werdelin, L., Chacón, M.G., Sala-Ramos, R., 2021. First small-sized *Dinofelis*: evidence from the Plio-Pleistocene of North Africa. *Quat. Sci. Rev.* 265, 107028.
- Malcres, O., Vernant, P., Fink, D., Cazes, G., Ritz, J.-F., Fujioka, T., Chéry, J., 2024. Cosmogenic nuclide-derived downcutting rates of canyons within large limestone plateaus of southern Massif Central (France) reveal a different regional speleogenesis of karst networks. *Earth Surf. Dyn.* 12, 679–690.
- Martin, L., Duval, M., Arnold, L.J., 2024. To what extent do field conditions affect gamma dose rate determination using portable gamma spectrometry? *Radiat. Phys. Chem.*, 111365 <https://doi.org/10.1016/j.radphyschem.2023.111365>.
- Martínez-Navarro, B., Karoui-Yaakoub, N., Oms, O., Amri, L., López-García, J.M., Zerai, K., Blain, H.-A., Mtifmet, M.S., Espigares, M.P., Haj Ali, N.B., Ros-Montoya, S., Bougħdiri, M., Agustí, J., Khayati-Ammar, H., Maalaoui, K., El Khir, M.H., Sala, R., Othmani, A., Hawas, R., Gómez-Merino, G., Palmqvist, P., 2014. The early Middle Pleistocene archeopaleontological site of Wadi Sarrat (Tunisia) and the earliest record of *Bos primigenius*. *Quat. Sci. Rev.* 90, 37–46.
- Martino, R., Rook, L., Mateus, O., Pandolfi, L., 2023. The Late Miocene hippopotamid, *Archaeopotamus pantanellii* nov. comb., from the Casino Basin (Tuscany, Italy): paleobiogeographic implications. *Hist. Biol.* <https://doi.org/10.1080/08912963.2023.2194912>.
- Matmon, A., Vainer, S., Hidy, A., Kuzmenko, A., Ekhhardt, F.E., Master, S., Wendorff, M., De Wit, M., Shaw, M., Team, A.S.T.E.R., Fink, D., Chazan, M., 2024. The Kalahari sediments and hominin in southern Africa. *Quat. Sci. Rev.* 334, 108716.
- Mein, P., Pickford, M., 1992. Gisements karstiques pléistocènes au Djebel Ressas, Tunisie. *C.R. Acad. Sci. Paris* 315, 247–253.
- Merchel, S., Bremser, W., 2004. First international ^{26}Al interlaboratory comparison - Part I. *Nucl. Instrum. Methods Phys. Res. Sect. B* 223–224, 393–400. <https://doi.org/10.1016/j.nimb.2004.04.076>.
- Monegatti, P., Raffi, S., 2001. Taxonomic diversity and stratigraphic distribution of Mediterranean Pliocene bivalves. *Palaeogeogr. Palaeoclimatol. Palaeoecol.* 165, 171–193.
- Nishiizumi, K., Imamura, M., Caffee, M.W., Sounthor, J.R., Finkel, R.C., McAninch, J., 2007. Absolute calibration of ^{10}Be AMS standards. *Nucl. Instrum. Methods Phys. Res. Sect. B Beam Interact. Mater. Atoms* 258, 403–413.
- Norris, T.L., Gancarz, A.J., Rokop, D.J., Thomas, K.W., 1983. Half-life of ^{26}Al . *J. Geophys. Res.* 88, B331–B333. Supplement.
- Ogg, J.G., 2020. Geomagnetic Polarity Time Scale. In: Ogg, G.M., eds., *Geologic Time Scale 2020*. Elsevier, Amsterdam, pp. 159–192. <https://doi.org/10.1016/B978-0-12-824360-2.00005-X>.
- Pappu, S., Gunnell, Y., Akhilesh, K., Braucher, R., Taieb, M., Demory, F., Thouveny, N., 2011. Early Pleistocene presence of Acheulian hominins in South India. *Science* 331, 1596–1599.
- Parés, J.M., Haddoumi, H., Duval, M., Álvarez-Posada, C., Aouraghe, H., Pla-Pueyo, S., Benito-Calvo, A., Rodríguez-Hidalgo, A., van der Made, J., Piñero, P., Agustí, J., Ouja, A., Grün, R., Chacón, M.G., Sala-Ramos, R., 2023. First magnetostratigraphic results in the Ain Beni Mathar-Guefiet Basin, Northern high plateaus (Morocco): the Dhar Iroumyane composite section. *Geobios* 76, 17–36. <https://doi.org/10.1016/j.geobios.2023.01.004>.
- Partridge, T.C., Granger, D.E., Caffee, M.W., Clarke, R.J., 2003. Lower Pliocene hominid remains from Sterkfontein. *Science* 300, 607–612.
- Pastor, A., Babault, J., Owen, L.A., Teixell, A., Arboleya, M.L., 2015. Extracting dynamic topography from river profiles and cosmogenic nuclide geochronology in the Middle Atlas and the High Plateaus of Morocco. *Tectonophysics* 663, 95–109.
- Piñero, P., Agustí, J., Haddoumi, H., El Hammouti, K., Chacón, M.G., Sala-Ramos, R., 2020. *Golunda aouraghei*, sp. nov., the last representative of the genus *Golunda* in Africa. *J. Vertebr. Paleontol.* 39, e1742726.
- Pla-Pueyo, S., Viseras, C., Soria, J.M., Tent-Manclús, J.E., Arribas, A., 2011. A stratigraphic framework for the Pliocene–Pleistocene continental sediments of the Guadix basin (Betic Cordillera, S. Spain). *Quat. Int.* 243 (1), 16–32.
- Pla-Pueyo, S., Gierowski-Kordesch, E.H., 2024. Wetlands as environments of early human occupation: a new classification for freshwater palaeowetlands. In: Benavente, C.A., Bohacs, K., Pla-Pueyo, S. (Eds.), *Water Pathways and Ancient Lakes: Flowing towards New Models to Unravel the Past*. The Depositional Record, 10.
- Prescott, J.R., Hutton, J.T., 1994. Cosmic ray contributions to dose rates for luminescence and ESR dating: Large depths and long-term time variations. *Radiat. Meas.* 23 (2–3), 497–500.
- Raffi, I., Wade, B.S., Pálki, H., 2020. The Neogene period. In: Gradstein, F.M., Ogg, J.G., Schmitz, M.D., Ogg, G.M. (Eds.), *Geologic Time Scale 2020*. Elsevier, Amsterdam, pp. 1141–1215.
- Ramírez-Pedraza, I., Tornero, C., Aouraghe, H., Rivals, F., Patalano, R., Haddoumi, H., Expósito, I., Rodríguez-Hidalgo, A., Mischke, S., van der Made, J., Piñero, P., Blain, H.-A., Roberts, P., Jha, D.K., Agustí, J., Sánchez-Bandera, C., Lemjidi, A., Benito-Calvo, A., Moreno-Ribas, E., Ouja, A., Mhamdi, H., Souhir, M., Aissa, A.M., Chacón, M.G., Sala-Ramos, R., 2024. Arid, mosaic environments during the Plio-Pleistocene transition and early hominin dispersals in northern Africa. *Nat. Commun.* 15 (1), 8393.
- Rink, W.J., Bartoll, J., Schwarcz, H.P., Shane, P., Bar-Yosef, O., 2007. Testing the reliability of ESR dating of optically exposed buried quartz sediments. *Radiation Measurements* 42 (10), 1618–1626.
- Rixhon, G., 2023. Deeper underground: cosmogenic burial dating of cave-deposited alluvium to reconstruct long-term fluvial landscape evolution. *Earth Sci. Rev.* 239, 104357.
- Rixhon, G., 2020. Plio-Quaternary landscape evolution in the uplifted Ardennes: new insights from $^{26}\text{Al}/^{10}\text{Be}$ data from cave-deposited alluvium (Meuse catchment, E. Belgium). *Geomorphology* 371, 107424.
- Rixhon, G., Bartz, M., El Ouahabi, M., Szemkus, N., Brückner, H., 2017. Contrasting terrace systems of the lower Moulouya river as indicator of crustal deformation in NE Morocco. *J. Afr. Earth Sci.* 126, 45–57.
- Robinson, P., Black, C.C., Krishalka, L., Dawson, M.R., 1982. Fossil small mammals from the Kechabta Formation, Northwestern Tunisia. *Ann. Carnegie Mus.* 51, 231–249.
- Rugel, G., Pavetich, S., Akhmadaliev, S., Enamorado Baez, S.M., Scharf, A., Ziegenrücker, R., Merchel, S., 2016. The first four years of the AMS-facility DREAMS: Status and developments for more accurate radionuclide data. *Nucl. Instrum. Methods Phys. Res., Sect. B* 370, 94–100. <https://doi.org/10.1016/j.nimb.2016.01.012>.
- Sahnouni, M., Parés, J.M., Duval, M., Cáceres, I., Harichane, Z., Van der Made, J., Pérez-González, A., Abdessadok, S., Kandi, N., Derradjai, A., Medig, M., Boulaghraif, K., Semaw, S., 2018. 1.9–2.4 million-year-old artefacts and stone tool cutmarked bones from Ain Boucherit. *Alger. Sci.* 362 (6420), 1297–1301. <https://doi.org/10.1126/science.aau0008>.
- Sala-Ramos, R., Aouraghe, H., Haddoumi, H., Morales, J.I., Rodríguez-Hidalgo, A., Tornero, C., Ouja, A., Bengamra, S., Soto, M., Farkouch, M., Aissa, El M., El Atmani, A., Duval, M., Arnold, L., Demuro, M., Blain, H.-A., Piñero, P., Rivals, F., Burjachs, F., Tarriño, A., Álvarez-Posada, C., Souhir, M., Saladié, P., Pla-Pueyo, S., Cruz Larrasoáñez, J., Mischke, S., Marín, J., Moreno-Ribas, E., De Lobmera-Hermida, A., Bartrolí, R., Lombao, D., García-Argudo, G., Ramírez, I., Díez-Canseco, C., Tomasso, S., Expósito, I., Allué, E., Hajji, N., Mhamdi, H., Rhosne, H., Carrancho, Á., Villalain, J.J., Van der Made, J., Canals, A., Benito-Calvo, A., Agustí, J., Parés, J.M., Chacón, M.G., 2022. Le peuplement humain pendant le Pléistocène et l'Holocène dans la Province de Jerada, Maroc Oriental: introduction d'un projet de recherche. *Bulletin d'Archéologie Marocaine* 27, 27–40.
- Stoetzel, E., 2013. Late Cenozoic micromammal biochronology of northwestern Africa. *Palaeogeogr. Palaeoclimatol. Palaeoecol.* 392, 359–381.
- Stone, J.O., 2000. Air pressure and cosmogenic isotope production. *J. Geophys. Res.* 105, 23753–23759.
- Tissoux, H., Falguères, C., Voinchet, P., Toyoda, S., Bahain, J.J., Despriée, J., 2007. Potential use of Ti-center in ESR dating of fluvial sediment. *Quat. Geochronol.* 2 (1–4), 367–372.
- Toyoda, S., 2015. Paramagnetic lattice defects in quartz for applications to ESR dating. *Quat. Geochronol.* 30, 498–505.
- Toyoda, S., Ikeya, M., 1991. Thermal stabilities of paramagnetic defect and impurity centers in quartz: Basis for ESR dating of thermal history. *Geochem. J.* 25, 437–445.
- Toyoda, S., Ikeya, M., 1994. ESR dating of quartz with stable component of impurity centers. *Quat. Sci. Rev.* 13 (5), 625–628.

- Toyoda, S., Falguères, C., 2003. The method to represent the ESR signal intensity of the aluminium hole center in quartz for the purpose of dating. *Adv. ESR Appl.* 20, 7–10.
- Toyoda, S., Voinchet, P., Falguères, C., Dolo, J.M., Laurent, M., 2000. Bleaching of ESR signals by the sunlight: a laboratory experiment for establishing the ESR dating of sediments. *Appl. Radiat. Isot.* 52 (5), 1357–1362.
- van der Made, J. et al. (in prep.). The Late Pliocene Large Vertebrate Fauna from Guefaït 4 (NE Morocco) and the Formation of the Saharo-Arabian Biogeographic Realm.
- van der Made, J., Boulaghraief, K., Chelli-Chehab, R., Duval, M., Parés, J.M., Cáceres, I., Semaw, S., Sahnouni, M., 2021. The North African earliest Pleistocene faunal sequence: from biostratigraphy to biochronology. *Mémoire du Service de Géologie de l'Algérie. Proc. QUATAL Workshop* 22, 73–90.
- van der Made, J., Boulaghraief, K., Chelli-Chehab, R., Cáceres, I., Harichane, Z., Sahnouni, M., 2022. The last North African hipparians – hipparion decline and extinction follows a common pattern. *Neues Jahrbuch für Geologie und Paläontologie, Abhandlungen* 303/1, 39–87.
- Vandenbergh, D., De Corte, F., Buylaert, J.P., Kučera, J., Van den haute, P., 2008. On the internal radioactivity in quartz. *Radiat. Meas.* 43 (2–6), 771–775.
- Voinchet, P., Falguères, C., Laurent, M., Toyoda, S., Bahain, J.J., Dolo, J.M., 2003. Artificial optical bleaching of the Aluminium center in quartz implications to ESR dating of sediments. *Quat. Sci. Rev.* 22 (10–13), 1335–1338.
- Voinchet, P., Toyoda, S., Falguères, C., Hernandez, M., Tissoux, H., Moreno, D., Bahain, J.J., 2015. Evaluation of ESR residual dose in quartz modern samples, an investigation on environmental dependence. *Quat. Geochronol.* 30, 506–512. Part B.
- Voinchet, P., Pereira, A., Nomade, S., Falguères, C., Biddittu, I., Piperno, M., Moncel, M.H., Bahain, J.J., 2020. ESR dating applied to optically bleached quartz - a comparison with $^{40}\text{Ar}/^{39}\text{Ar}$ chronologies on Italian Middle Pleistocene sequences. *Quat. Int.* 556, 113–123.
- Wen, X., Bartz, M., Schmidt, C., King, G.E., 2024. ESR and luminescence thermochronometry of the Rhône valley, Switzerland. *Quat. Geochronol.* 80, 101496.
- Werdelin, L., 2003. Mio-pliocene Carnivora from Lothagam, Kenya. In: Leakey, M.G., Harris, J.D. (Eds.), *Lothagam: Dawn of Humanity in Eastern Africa*. Columbia University Press -, New York, pp. 261–328.
- Werdelin, L., 2010. Chronology of Neogene mammal localities. In: Werdelin, L., Sanders, W.J. (Eds.), *Cenozoic Mammals of Africa*. University of California Press -, Berkeley, Los Angeles, London, pp. 27–43.
- White, T.D., 1996. African omnivores: global climatic change and Plio-Pleistocene hominids and suids. In: Vrba, E.S., Denton, D.H., Partidge, T.C., Burckle, L.H. (Eds.), *Paleoclimate and Evolution, with Emphasis on Human Origins*. Yale University Press, New Haven & London, pp. 369–384.
- Woda, C., Wagner, G.A., 2007. Non-monotonic dose dependence of the Ge- and Ti-centres in quartz. *Radiat. Meas.* 42 (9), 1441–1452.
- Xu, X., Wei, C., Yin, G., Ji, H., Liu, C., Zhao, L., Yang, H., Yang, G., 2024. Application of multiple-centers ESR dating to middle Pleistocene fluviolacustrine sediments and insights into the dose underestimation from the Ti-H center at high equivalent doses. *Quaternary Geochronology* 85, 101635.
- Zouhri, S., Amane, A., 2022. Updated Neogene mammalian biochronology and biogeography of Morocco. *Hist. Biol.* 34 (8), 1611–1622.
- Zouhri, S., Benammi, M., Geraads, D., El Boughabi, S., 2017. Mammifères du Néogène continental du Maroc: Faunes, biochronologie et paléobiogéographie. *Mémoires de la société Géologique de France* 180, 527–588.